

Constraining physical conditions for the PDR of Trumpler 14 in the Carina Nebula[★]

Ronin Wu^{1,2}, Emeric Bron^{1,3}, Takashi Onaka², Franck Le Petit¹, Frédéric Galliano⁴, David Languignon¹, Tomohiko Nakamura^{2,5}, and Yoko Okada⁶

¹ LERMA, Observatoire de Paris, PSL Research University, CNRS, Sorbonne Universités, UPMC Univ. Paris 06, F-92190, Meudon, France; e-mail: ronin.wu@obspm.fr

² Department of Astronomy, the University of Tokyo, Bunkyo-ku, Tokyo 113-0033, Japan

³ Grupo de Astrofísica Molecular. Instituto de Ciencia de Materiales de Madrid (ICMM, CSIC), Sor Juana Ines de la Cruz 3, 28049 Cantoblanco, Madrid, Spain

⁴ IRFU, CEA, Université Paris-Saclay, F-91191 Gif-sur-Yvette, France

Université Paris-Diderot, AIM, Sorbonne Paris Cité, CEA, CNRS, F-91191 Gif-sur-Yvette, France

⁵ Recruit Communications Co. Ltd, Tokyo, Japan

⁶ I. Physikalisches Institut der Universität zu Köln, Zùlpicher Strasse 77, 50937 Köln, Germany

June 9, 2022

ABSTRACT

We investigate the physical conditions of the CO gas, based on the submillimeter imaging spectroscopy from a $2' \times 7'$ ($1.5 \times 5 \text{ pc}^2$) area near the young star cluster, Trumpler 14 of the Carina Nebula. The observations presented in this work are taken with the Fourier Transform Spectrometer (FTS) of the Spectral and Photometric Imaging REceiver (SPIRE) onboard the *Herschel* Space Observatory. The newly observed spectral lines include [C_I] $370 \mu\text{m}$, [C_I] $609 \mu\text{m}$, and CO transitions from $J = 4 - 3$ to $J = 13 - 12$. Our field of view covers the edge of a cavity carved by Trumpler 14 about 1 Myr ago and marks the transition from H_{II} regions to photo-dissociation regions. The observed CO intensities are the most prominent at the northwest region, Car I-E. With the state-of-the-art Meudon PDR code, we successfully derive the physical conditions, which include the thermal pressure (P) and the scaling factor of radiation fields (G_{UV}), from the observed CO spectral line energy distributions (SLEDs) in the observed region. The derived G_{UV} values generally show an excellent agreement with the UV radiation fields created by nearby OB-stars and thus confirm that the main excitation source of the observed CO emission are the UV-photons provided by the massive stars. The derived thermal pressure is between $0.5 - 3 \times 10^8 \text{ K cm}^{-3}$ with the highest values found along the ionization front in Car I-E region facing Trumpler 14, hinting that the cloud structure is similar to the recent observations of the Orion Bar. We also note a discrepancy at a local position ($< 0.17 \times 0.17 \text{ pc}^2$) between the PDR modeling result and the UV radiation fields estimated from nearby massive stars, which requires further investigation on nearby objects that could contribute to local heating, including outflow. Comparing the derived thermal pressure with the radiation fields, we report the first observationally-derived and spatially-resolved $P \sim 2 \times 10^4 G_{\text{UV}}$ relationship. As direct comparisons of the modeling results to the observed ^{13}CO , [O_I] $63 \mu\text{m}$, and [C_{II}] $158 \mu\text{m}$ intensities are not straightforward, we urge the readers to be cautious when constraining the physical conditions of PDRs with combinations of ^{12}CO , ^{13}CO , [C_I], [O_I] $63 \mu\text{m}$, and [C_{II}] $158 \mu\text{m}$ observations.

Key words. ISM: individual objects: Carina Nebula – Interstellar medium (ISM), nebulae – ISM: clouds – ISM: molecules – ISM: structure – (Galaxy:) open clusters and associations: individual: Trumpler 14

1. Introduction

The radiative feedback of stars on their parent cloud is a key topic both in the context of evolution and composition of interstellar matter and to constrain star formation mechanisms. Emission lines from photo-dissociation regions (PDRs) have been studied for decades to understand the physical and chemical processes induced by this feedback (Tielens & Hollenbach 1985; Sternberg & Dalgarno 1989). In these regions, far ultraviolet (FUV) photons dissociate molecules and heat the gas at several hundred Kelvins via photo-electric effect on grains and, in dense gas, by H₂ pumping followed by collisional de-excitations (Röllig et al. 2006). Several tracers are commonly used to study PDRs. Observations of atomic lines of O, C⁺ and C probe the

neutral hydrogen layer and give access to most of the gas cooling rate at the edge of the cloud. The atomic-molecular transition can be observed thanks to the emission of H₂ infrared lines. Less abundant molecules, diatomic and complex ones as carbon chains, formaldehyde or methanol, have been detected at various depths in PDRs showing that complex chemistry takes place in this hostile environment (Young Owl et al. 2000; Lis & Schilke 2003; Guzmán et al. 2013; Nagy et al. 2013; Guzmán et al. 2014; Cuadrado et al. 2015). Because H₂ is difficult to observe, except at the warm surface layer of cloud, due to its lack of electric dipole moment, many studies rely on the observation of CO and its isotopologs to constrain the mass of gas and the morphology of clouds.

Since its launch in 2009, *Herschel* Space Observatory (Pilbratt et al. 2010) has allowed Galactic and extragalactic observations of excited CO in high-J states ($J_{\text{up}} > 10$) in PDRs of various objects (Köhler et al. 2014; Stock et al. 2015; Wu et al. 2015;

[★] *Herschel* is an ESA space observatory with science instruments provided by European-led Principal Investigator consortia and with important participation from NASA.

Parikka et al. 2017). In parallel, observations of CO emission in protostars and extragalactic environments showed highly excited CO. For example, emission from rotational levels $J_{\text{up}} > 40$ has been observed in the protostellar region Orion BL/KL, suggesting an excitation by outflows and shocks (Goicoechea et al. 2015). In extragalactic regions, the origin of CO excitation is unclear (Yıldız et al. 2010; Hailey-Dunsheath et al. 2012; Greve et al. 2014; Kamenetzky et al. 2016; Rosenberg et al. 2015). Candidate excitation sources include mechanical-heating, shocks, X-rays, and UV photons, depending on the objects and the adopted tools in the analyses. It has been a topic of interest whether it is possible to infer the UV radiation field intensity and star formation rate from high-J CO line intensities. The study of CO excitation in spatially resolved Galactic PDRs can help to answer this question. Presently, most analyses rely on the usage of non-local thermal equilibrium (non-LTE) radiative transfer codes, such as large velocity gradient (LVG) approximations, to infer gas density and temperature from CO line intensities (Köhler et al. 2014). Very few detailed analyses based on PDR modeling, which constrains the thermal and chemical processes hidden behind the observed CO lines, can be found in the literature. Based on the non spatially-resolved CO observations from $J = 4 - 3$ up to $J = 19 - 18$ in NGC 7023 and up to $J = 23 - 22$ in the Orion Bar, as well as other atomic and molecular lines, and their comparisons with the Meudon PDR code (Le Petit et al. 2006), it is suggested that the FUV radiation field produced by the Trapezium stars cluster and HD 200775 are responsible for a high pressure layer ($P \sim 10^8 \text{ K cm}^{-3}$) at the very edge of the two PDRs and is sufficient to support the high-J CO excitation observed in the two objects (Joblin et al. in prep.). These results are in resonance with the recent ALMA observations which confirm the presence of a thin layer with high pressure at the edge of the PDR in the Orion Bar (Goicoechea et al. 2016; Goicoechea et al. 2017). More studies as such with detailed PDR modeling are necessary for understanding the excitation of CO in the interstellar environment.

Another well known object that is suitable for studying the impact of radiative feedback of massive stars on their parent cloud is the Carina Nebula. Located at a close distance, 2.3 kpc (Smith 2006b), from us in the Milky Way, the Carina Nebula is the largest and brightest nebula in the southern sky. Some of its central regions are even brighter than the famous Orion Nebula. Aside from the famous luminous blue variable, η Carinae (η Car), Carina Nebula hosts 70 known O stars, 3 Wolf-Rayet stars, and 127 B0 to B3 stars (Gagné et al. 2011).

It was first revealed in the observations of radio continuum at 6 cm that the HII regions of the Carina Nebula include two major components, Car I and Car II, separated by $\sim 10'$ ($\sim 7 \text{ pc}$) along the Galactic plane (McGee & Gardner 1968; Gardner & Morimoto 1968). Based on the distribution of local maxima of radio continuum brightness at 0.843 GHz, Whiteoak (1994) detailed the structure of Car I into Car I-W, Car I-E, and Car I-S, which are associated to the ionization front shaped by the UV-photons from Trumpler 14 in the west, east and south of Car I. With the NASA Kuiper Airborne Observatory (KAO) far-infrared (FIR) and Fleurs Synthesis Telescope (FST) 1415 MHz observations, it is confirmed that the main heating sources for Car I and Car II are Trumpler 14 and Trumpler 16, respectively (Harvey et al. 1979; Retallack 1983). Figure 1 gives an overview of the north region of the Carina Nebula observed by the UK Schmidt Tele-

scope in the R-band of the Second Digital Sky Survey (DSS2 red)¹.

In this paper, we study the CO and C emission observed by *Herschel* SPIRE/FTS across an HII-PDR interface located at the northwest in the Carina Nebula to better understand the origin of CO excitation in PDRs as well as the impact of radiative feedback of massive stars. The observed region (enclosed by the white square in Figure 1) covers Car I-E (upper right), Car I-S (center), and a small region at the intersection of Car I and Car II (Car I/II, lower left, see also Figure 2 for the region definition). Our field-of-view (FOV) covers the edge of a cavity likely shaped by the young ($1 - 2 \text{ Myr}$) OB-star cluster Trumpler 14 since $\sim 1 \text{ Myr}$ ago with its ionization front sitting at a projected distance of $\sim 2 \text{ pc}$ from Trumpler 14.

Trumpler 14 hosts a dozen of O-stars and more than a hundred of B-stars. Its stellar components have been well studied (Vazquez et al. 1996; Carraro et al. 2004). The estimated UV input by the stellar members of Trumpler 14 to the ionization front of PDR is $\approx 10^4 G_0$ (Brooks et al. 2003) where $G_0 = 1.6 \times 10^{-3} \text{ erg s}^{-1} \text{ cm}^{-2}$ according to Habing (1968) (hereafter, the Habing unit). For comparison, this FUV flux is slightly lower than the one induced by the Trapezium star cluster on the famous Orion Bar ($\sim 3 \times 10^4 G_0$, Goicoechea et al. 2015) and comparable to the one found in extragalactic starburst regions (Malhotra et al. 2001; Chevance et al. 2016). Even though the FUV flux is similar between the Carina Nebula and the Orion Bar, the distance of the Trapezium star cluster to the Bar is ~ 10 times closer than in the Carina Nebula. As Trumpler 14 is a more evolved star cluster than the Trapezium star cluster, the interaction zones at its PDR interface can be better approximated by pressure equilibrium in a stationary PDR model (Brooks et al. 2003). Within the dense molecular gas at the northwest region, young stellar objects (YSOs) are carving out ionized regions anew, proving the on-going and active star formation in this region (Tapia et al. 2015). Such a region is likely a representation of prototypical PDRs near star-forming sites that dominate the extragalactic observations of starburst systems where individual PDRs are mostly unresolved in the infrared and submm.

The PDRs in the Car I-E region have thus far been studied by several groups. The FUV flux in this region, as estimated from stellar composition and FIR observations, is $\sim 10^4$ in the Habing unit (Brooks et al. 2003; Mizutani et al. 2004). However, estimations with PDR models have given somehow lower values of FUV flux (1390, Oberst et al. 2011 and 3200, Kramer et al. 2008 in the Habing unit). In a big picture, these results indicate that the UV-photons provided by nearby massive stars are more than sufficient in supporting the global heating of PDRs observed in this region. However, the inconsistency persists between the model-estimated values of FUV flux and the UV radiation fields estimated from stellar composition and FIR observations.

In this work, we adopt a distance of $2.35 \pm 0.5 \text{ kpc}$ to the Carina Nebula (Smith 2006b), although it is worth noting that the photometric analysis from pre-main sequence (PMS) stars in the nebula gives a distance of $\sim 2.9 \text{ kpc}$ to the star clusters, Trumpler 14 and 16 (Hur et al. 2012). All the sky coordinates

¹ Based on photographic data obtained using The UK Schmidt Telescope. The UK Schmidt Telescope was operated by the Royal Observatory Edinburgh, with funding from the UK Science and Engineering Research Council, until 1988 June, and thereafter by the Anglo-Australian Observatory. Original plate material is copyright (c) of the Royal Observatory Edinburgh and the Anglo-Australian Observatory. The plates were processed into the present compressed digital form with their permission. The Digitized Sky Survey was produced at the Space Telescope Science Institute under US Government grant NAG W-2166.

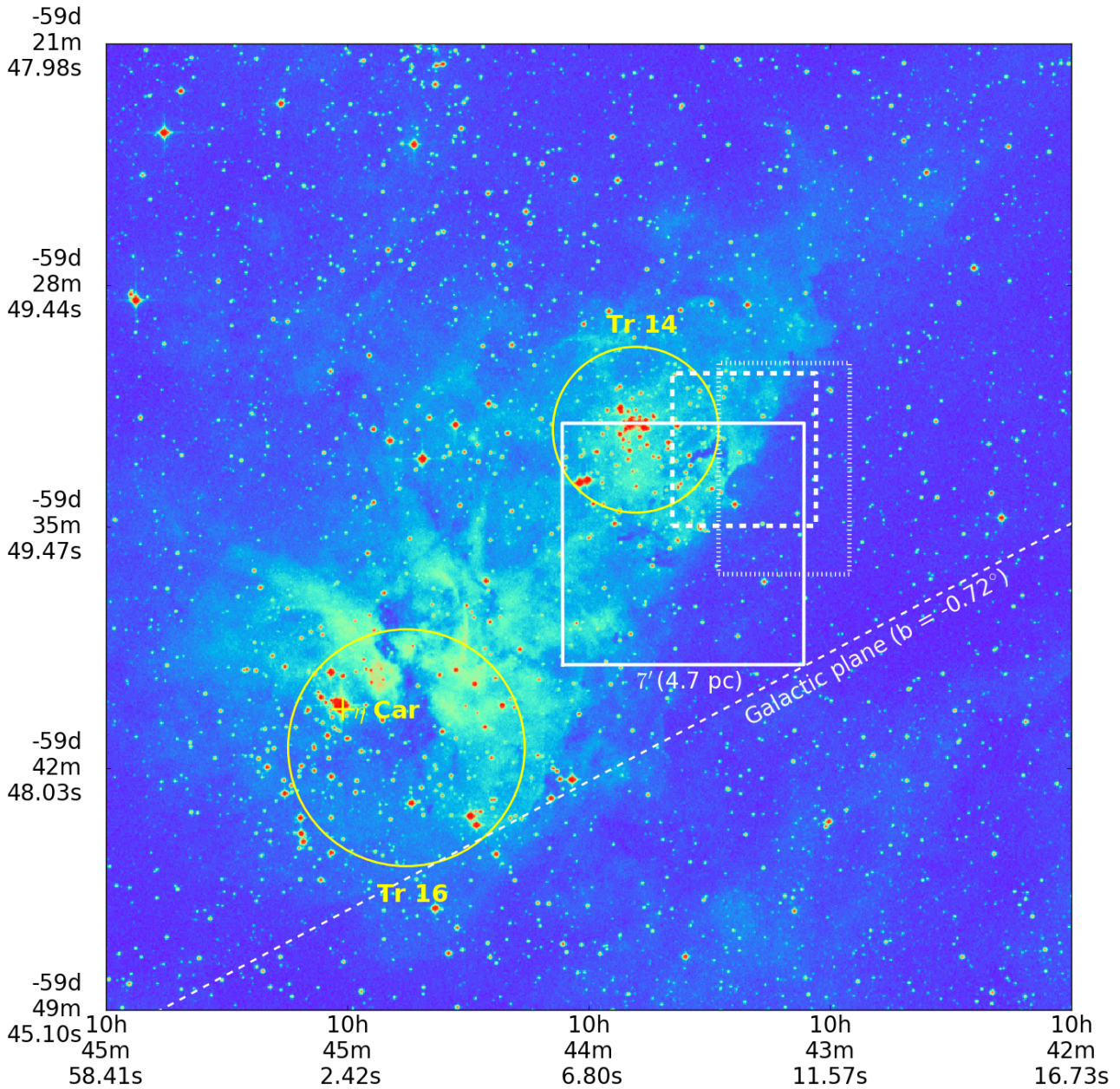


Fig. 1: Overview of the region north of the dust-lane in the Carina Nebula. The background optical image is taken with the UK Schmidt Telescope in the DSS2-red band. The locations and sizes of the two most massive star-clusters, Trumpler 14 and Trumpler 16, are marked with yellow circles (Tapia et al. 2003). The areas enclosed by the white dotted and dashed lines indicate the regions previously observed by Brooks et al. (2003) and Kramer et al. (2008). The long dashed line across the image marks the Galactic plane at $b = -0.72^\circ$. The square enclosed by the solid white line indicates the FOV in this work. It spans an area of $7' \times 7'$ (4.7×4.7 pc). A zoom-in view of the area included in the white square can be found in Figure 2.

quoted in this work are in the J2000 epoch. In the model analysis, we adopt the scaling factor according to the radiation field given by Mathis et al. (1983) (hereafter, the Mathis unit) unless otherwise specified. The difference between the Habing and Mathis units is about a factor of 1.3, in the spectral range of 91.2 to 111 nm. Our observations and data reduction procedure are presented in section 2. We interpret these data with the Meudon

PDR code in section 3. Results are then presented and discussed in sections 4 and 5, respectively.

2. Observations

The *Herschel* data presented in this work have been observed on 2012-12-03 and 2013-02-04 as one of the Open Time (OT1) programs (P.I.: Takashi Onaka). Our results are mainly derived from

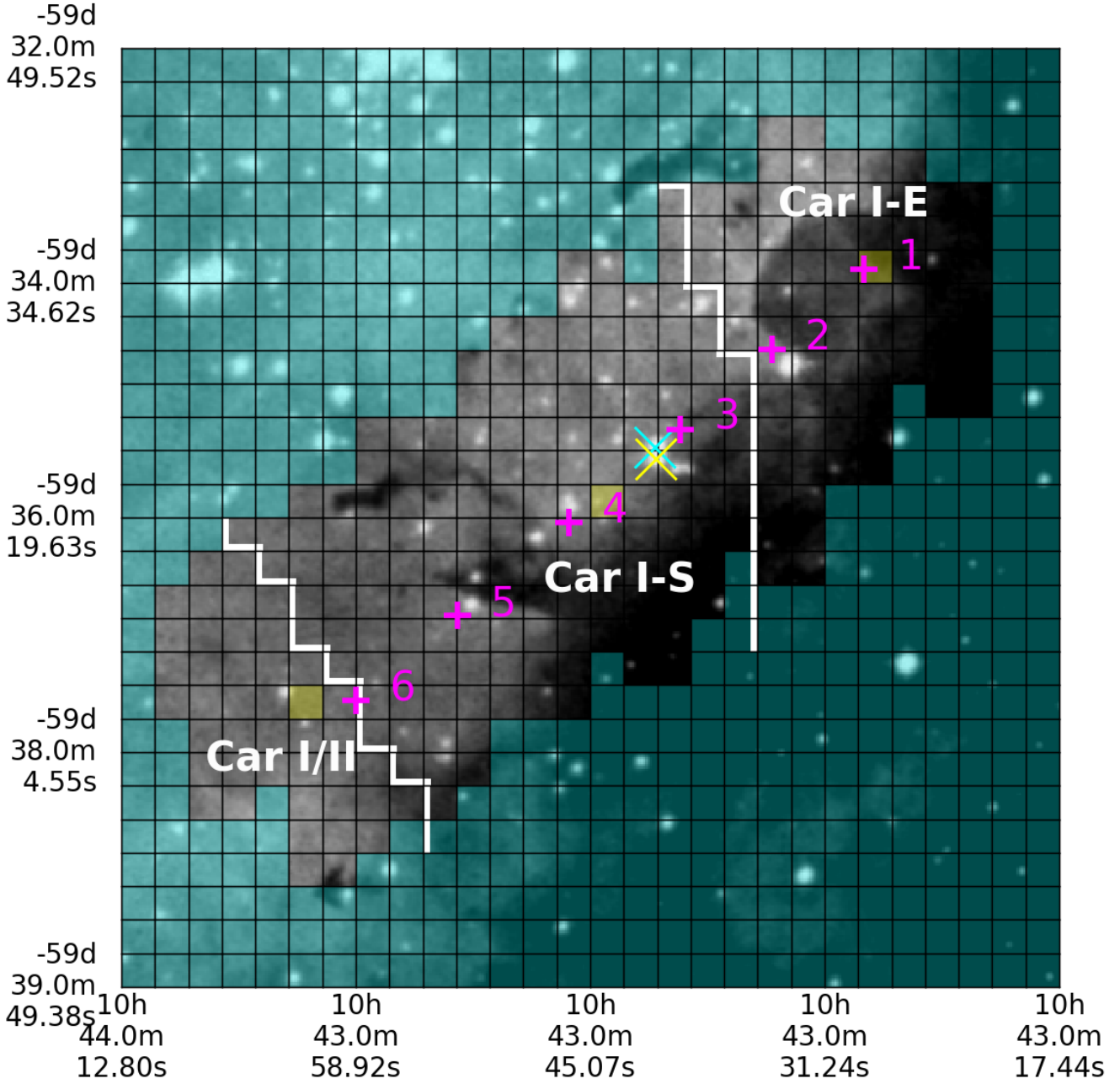


Fig. 2: A zoom-in of our FOV (the white square in Figure 1). The effective FOV is indicated by the pixels in gray-colors. The background image is the optical image taken in the DSS2-red band. The positions of the central bolometer, SLWC4, at the six requested pointings are indicated with the magenta crosses and labeled accordingly as in Table 1. The boundaries of Car I-E, Car I-S, and Car I/II areas are indicated with the thick white lines. The locations of two massive stars, *ALS 15 204* and *ALS 15 203*, discussed in Section 4.2 are marked with the cyan and yellow “x” in the figure. The CO SLED observed from the three yellow-masked pixels are displayed in Figure 8 and discussed in Section 5.1.

the spectroscopic data observed by the *Fourier Transform Spectrometer* (FTS) of the *Spectral and Photometric Imaging Receiver* (SPIRE, Griffin et al. 2010) on board the *Herschel Space Observatory* (Pilbratt et al. 2010). We give a brief instrumentation overview of the *Herschel* SPIRE/FTS, and then layout the steps we take to map the observations.

2.1. An overview of the *Herschel* SPIRE/FTS

The *Herschel* SPIRE/FTS is made of two bolometer arrays, the SPIRE Short Wavelength (SSW, 194 – 324 μm) and SPIRE Long Wavelength (SLW, 316 – 672 μm) arrays. Each of the SSW and SLW arrays, respectively, packs 19 and 7 unvignetted bolometers hexagonally on the focal plane and simultaneously covers a 2.6' diameter of field of view (FOV) on the sky. Our observa-

tions have been completed in six single-pointings on the operational days 1299 and 1362. At each single-pointing position, we observe the sky in the intermediate spatial-sampling (4 jiggle-pointings) and high spectral-resolution ($\Delta\sigma = 0.04 \text{ cm}^{-1}$ or $\Delta\nu = 1.2 \text{ GHz}$) modes. The information of our observation is listed in Table 1. For each jiggle-pointing, the sky has been observed in 8 scans, which add up to an effective exposure time of approximately 266 s across the FOV. The spectra presented in this work are calibrated against Uranus, *i.e.* point-source calibrated, using the SPIRE calibration tree, `spire_cal_14_3`. Details of the SPIRE/FTS calibration can be found in Swinyard et al. (2014). Beginning with the unapodized spectra, averaged from all scans, and their standard-deviation as the uncertainties, we describe our map-making strategy in the following subsection.

2.2. Making maps of the Herschel SPIRE/FTS lines

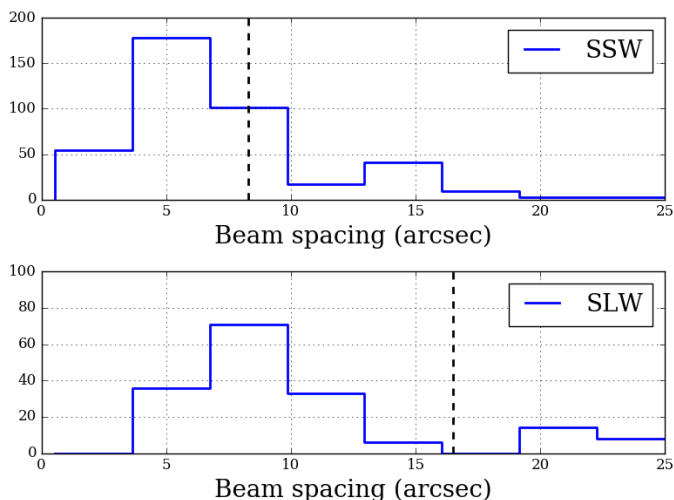


Fig. 3: Histograms of the distances for a given bolometer to its closest neighbor for the SSW (top) and SLW (bottom) arrays. The dashed lines mark half of the smallest beam FWHM listed in Table 2, which correspond to $8.3''$ and $16.5''$ for the SSW and SLW arrays respectively.

In the intermediate-sampling mode, the bolometer spacings for the SSW and SLW arrays are respectively $16.3''$ and $25.3''$, which are about the sizes of individual beams at their minimum within the bandwidths. Although the individual single-pointing observation used in this work is not fully-Nyquist sampled, combining the footprints of bolometers from all six single-pointing positions (see Figure 2), the average bolometer spacings in our FOV achieve $8.6''$ and $12.2''$ for SSW and SLW arrays respectively. Histograms of distances between any given bolometer to its closest neighbor for SSW and SLW arrays are shown in Figure 3, and they demonstrate that the observation within the effective FOV is approximately fully-Nyquist sampled.

Within the bandwidth ($194 < \lambda < 672 \mu\text{m}$) of the *Herschel* SPIRE/FTS, the relevant atomic and molecular lines used in this study are listed in Table 2. As discussed in Wu et al. (2013) and Swinyard et al. (2014), the beam full-width-half-maxima (FWHM) and sensitivities of bolometers vary across the instrument bandwidth. At each observed emission line, we list the correspondent instrument FWHM and mean 1σ uncertainty of the integrated line intensity (ϵ) in Table 2.

Around the frequency ($\nu_{\text{line}} - 15 \text{ GHz} < \nu < \nu_{\text{line}} + 15 \text{ GHz}$) of each line listed in Table 2, the observed spectra from all unvignetted bolometers are assigned to a regular-grid map. The world coordinate system (WCS) of the maps is centered at $(\alpha, \delta) = (10:43:45.07, -59:36:19.63)$ with each pixel sized $15'' \times 15''$ ($0.17 \times 0.17 \text{ pc}$) and a total dimension of $7'' \times 7''$ ($4.7 \times 4.7 \text{ pc}$). We follow a similar map-making recipe detailed in § 2.1.2 of Wu et al. (2015) and briefly discuss the main steps here. The stand-alone map-making software, `HFTS_mapping`, is written in Python and uses utilities publicly available in `astropy`² (version 1.1.1, Robitaille et al. 2013), `scipy` (version 0.17.0) and `numpy` (version 1.12.1)³. `HFTS_mapping` is now available for public use⁴.

Our map-making procedure can be laid out in three steps:

- First, before coadding the level-2 bolometer spectra on the map, a continuum level is estimated between two frequency-intervals, ($\nu_{\text{line}} - 15 \text{ GHz} < \nu < \nu_{\text{line}} - 5 \text{ GHz}$) and ($\nu_{\text{line}} + 5 \text{ GHz} < \nu < \nu_{\text{line}} + 15 \text{ GHz}$), and removed as a parabola function. Weighted by the uncertainties, which are estimated as the standard deviation from all scans, the continuum-removed bolometer spectra are then assigned to the pixels, according to the bolometer pointings, to create spectral cubes over the FOV for each line listed in Table 2.
- Second, we measure the integrated line-intensity, assuming a sinc profile, from spectral cubes constructed in the previous step. For CO $J = 7 - 6$ and $[\text{C}]\text{P}_1 - ^3\text{P}_2$, which are only 2.7 GHz apart, their integrated line-intensities are measured simultaneously with two sinc profiles whose central frequencies are fixed to differ by 2.7 GHz . At the end of this step, the maps of integrated line-intensities are produced (see figures in Appendix A).
- The last step of map-making is to convolve the integrated line-intensity maps to the same spatial resolution, $42''$ ($\sim 0.5 \text{ pc}$), which is the largest beam FWHM among all observed lines (see Table 2). We refer the curious readers to Wu et al. (2015) for more detailed description on the generation of kernels used in convolution.

Uncertainties for the final integrated line-intensities are estimated by a Monte-Carlo experiment which comprises 300 repetitions of the above three steps. For each repetition, the uncertainties used for coaddition of bolometer spectra in the first step are replaced by randomly generated noises which include random and systematic uncertainties from the observation. The random uncertainties are represented by a normal distribution whose standard-deviation is the root-mean-square (rms) of residuals from a given bolometer spectrum after subtracting its continuum and the sinc line-profile(s).

For all bolometer spectra taken in the same single-pointing observation, one normal distribution that represents the systematic uncertainty has also been taken into account. The $1-\sigma$ of the normal distribution for the systematic uncertainty is set to be 10% of the bolometer spectrum (Swinyard et al. 2014). The uncertainties used in the first step are then replaced by the rms of the generated random and systematic uncertainties. At the end of the Monte Carlo experiment, 300 convolved maps of integrated line-intensities for each line are produced. For a given line on each pixel, the standard-deviation between the 300 maps is taken as the final uncertainty.

² <http://www.astropy.org/>

³ <https://www.scipy.org/>

⁴ https://ism.obspm.fr/files/HFTS_Mapping/HFTS_mapping_20171220.tgz

Table 1: The *Herschel* SPIRE/FTS observations presented in this work.

Pointing label	Obs_ID	RA (J2000)	Dec (J2000)	Obs. Time	Note
1	1342262913	10:43:29.08	-59:34:29.96	2013-02-04 06:46:20	C
2	1342262914	10:43:34.47	-59:35:05.56	2013-02-04 07:24:13	C'
3	1342262915	10:43:39.85	-59:35:41.59	2013-02-04 08:02:06	SWS
4	1342262916	10:43:46.45	-59:36:23.36	2013-02-04 08:39:59	B'
5	1342256377	10:43:53.05	-59:37:04.77	2012-12-03 13:39:48	B
6	1342256376	10:43:59.03	-59:37:42.62	2012-12-03 13:01:54	A

Notes. The pointing labels are according to the positions indicated in Figure 2. The Obs_ID is the unique identifier for *Herschel* observations. The labels used in Onaka et al. (2008) are given in the Note column.

Within our FOV, the CO $J = 4 - 3$ and $J = 7 - 6$ transitions have previously been observed with the 4 m NANTEN2 telescope. The FWHMs of the NANTEN2 observations are $38''$ and $26.5''$ for the CO $J = 4 - 3$ and $J = 7 - 6$ transitions, respectively, with 20% of calibration uncertainty (Kramer et al. 2008). After convolving the CO $J = 4 - 3$ and $J = 7 - 6$ images observed by NANTEN2 to the instrument FWHM of the *Herschel* SPIRE/FTS, the data observed by the two telescopes show agreement within 30%.

3. Data interpretation

We deduce the physical conditions at each pixel with version 1.5.2 of the Meudon PDR code (Le Petit et al. 2006), which is available on the ISM Services webpage⁵ of Paris Observatory. In this section, we first give an overview on the Meudon PDR code and discuss the strategies adopted in the data interpretation.

3.1. The Meudon PDR code

The Meudon PDR code computes chemical densities and gas excitation in a 1-D stationary plane-parallel slab of gas and dust illuminated by a radiation field. At each point of the spatial grid, the code consistently solves the radiative transfer, the chemistry and the thermal balance, which computes individually the heating and cooling mechanisms. The chemical network used in this paper includes 224 species and 6311 chemical reactions.

H₂ formation on grains is a key process since it controls the transition between the neutral atomic and the molecular phases. The default prescription in the Meudon PDR code simulates the H₂ formation on dust grains through Eley-Rideal and Langmuir-Hinshelwood mechanisms, as described in Le Bourlot et al. (2012). Although a more sophisticated and computing time-demanding H₂ formation prescription that simulates the stochastic heating of grains by UV photons, its effect on the H₂ formation, and ortho/para conversion, on the grain surfaces is also available (Bron et al. 2014, 2016), we opt for the Le Bourlot et al. (2012) prescription to gain efficiency in computing time.

At each point of the spatial grid, the radiative transfer equation is solved considering absorption and diffusion by dust as well as absorption in continuum of some gas species as C. Self-shielding for critical species, such as H₂ and CO, is computed with the Federman et al. (1979) formalism (see Le Petit et al. 2006 for details).

The most important heating processes taken into account are the photo-electric effect on grains (Bakes & Tielens 1994), heating by collisional de-excitation of H₂, and cosmic rays as well as exothermic reactions. As for the cooling processes, the non-LTE

level excitation of main coolants is computed at each position in the cloud, considering various micro-physical processes, such as collisions and radiative (de-)excitation (Gonzalez Garcia et al. 2008).

Another important aspect is the treatment of grains. Grains impact the photo-electric heating rate, the penetration of UV photons, the IR dust emission, and the formation of H₂. In the models used for this work, a MRN-like grain size distribution (Mathis et al. 1977) is adopted for carbonaceous grains and silicates, plus a log-normal distribution for polycyclic aromatic hydrocarbons (PAHs). The photo-electric heating from PAHs is estimated with the prescriptions given in Bakes & Tielens (1994). For every model, the code simulates and outputs detailed thermal (gas and grains) and chemical (with level excitation for selected species) structures of the cloud, as a function of depths, as well as the integrated quantities, such as column densities and line intensities.

For this work, a non-uniform grid of 1367 PDR models has been produced. The explored physical space is the thermal pressure, the intensity of incident UV radiation fields and the depth of the cloud. The thermal pressure, P , ranges from 10^5 to 10^9 K cm⁻³. The UV field scaling factor, G_{UV} , ranges from 1 to 10^5 in the Mathis units (Mathis et al. 1983). The visual extinction, A_V goes from 1 to 40 magnitudes. Other parameters, common to all models are presented in Tables 3 and 4. These models are available in the Interstellar Medium Data Base (ISMDB)⁶ at <http://ismdb.obspm.fr>.

3.2. Modeling strategy

Alongside the transitions listed in Table 2, observations of [CII] 158 μ m, [OI] 63 and 145 μ m with the *Herschel* Photodetector Array Camera and Spectrometer (PACS, Poglitsch et al. 2010) as well as the ¹³CO transitions covered by the *Herschel* SPIRE/FTS bandwidth ($J = 5 - 4$ to $J = 14 - 13$) are also available. The Meudon PDR code can simulate line-intensities of all these transitions. That is, a priori, all of them could be used to find the best model that matches the observations. Nevertheless, we use only the CO and C lines listed in Table 2 to constrain the physical parameters based on the following three reasons.

First, it is not yet clear whether the atomic emissions associated with C⁺ and O share the same origin with the observed CO and C transitions. A comparison of line profiles, resolved both spectrally and spatially, of [CII] 158 μ m and CO transitions ($J = 2 - 1$, $J = 6 - 5$, and $J = 13 - 12$) in M17 SW shows that the emissions of C⁺ and CO are hardly associated in their distributions (Pérez-Beaupuits et al. 2012). Spectrally-resolved observations of G5.89 – 0.39, a massive star-forming region in

⁵ <http://ism.obspm.fr>

⁶ The ID of the grid of models in ISMDB is DM54.

Table 2: Emission lines used to constrain the physical conditions and observed by the *Herschel* SPIRE FTS.

Transition	Frequency (GHz)	E_{up} (K)	g_{up}	FWHM ($''$)	ϵ ($10^{-9} \text{ W m}^{-2} \text{ sr}^{-1}$)
CO J = 4 – 3	461.041	55.32	9	41.7	1.40
[C I] $^3\text{P}_0 - ^3\text{P}_1$	492.161	23.62	3	38.1	0.84
CO J = 5 – 4	576.268	82.97	11	33.5	1.27
CO J = 6 – 5	691.473	116.16	13	29.3	1.02
CO J = 7 – 6	806.652	154.87	15	33.0	1.02
[C I] $^3\text{P}_1 - ^3\text{P}_2$	809.342	62.46	5	33.0	1.01
CO J = 8 – 7	921.800	199.11	17	33.2	1.88
CO J = 9 – 8	1036.912	248.88	19	19.1	2.22
CO J = 10 – 9	1151.985	304.16	21	17.6	2.53
CO J = 11 – 10	1267.015	364.97	23	17.3	2.65
CO J = 12 – 11	1381.995	431.29	25	16.9	2.52
CO J = 13 – 12	1496.923	503.13	27	16.6	4.37

Notes. The two last columns correspond to the instrument FWHM and to the mean 1σ uncertainty of the integrated line intensity.

Table 3: Common parameters used for the grid of PDR models.

Quantity	value	unit	note
ζ	10^{-16}	s^{-1}	(1)
$N_{\text{H}} / E(\text{B-V})$	5.8×10^{21}	$\text{cm}^{-2} \text{ mag}^{-1}$	(2)
$m_{\text{grain}} / m_{\text{gas}}$	0.01	no unit	(3)
α	-3.5	no unit	(4)
a_{min}	1×10^{-7}	cm	(5)
a_{max}	3×10^{-5}	cm	(6)
$m_{\text{PAH}} / m_{\text{grain}}$	4.6×10^{-2}	no unit	(7)

Notes. (1): cosmic-ray ionization rate of H_2 per second. (2) Gas-to-grain ratio (Bohlin et al. 1978). (3) grain to gas mass ratio. (4) MRN power law exponent. (5) minimum radius of grains. (6) maximum radius of grains. (7) PAH to grain mass ratio.

Table 4: Elementary abundances used in the chemical network.

Elements	Value	Element	Value
O/H	3.2×10^{-4}	D/H	1.5×10^{-5}
C/H	1.3×10^{-4}	$^{13}\text{C}/\text{H}$	1.9×10^{-6}
N/H	7.5×10^{-5}	$^{18}\text{O}/\text{H}$	5.7×10^{-7}
S/H	1.9×10^{-5}		

our Galaxy, have also shown a difference between the velocity distributions of [OI] $63 \mu\text{m}$ and the CO transitions ($J = 7 - 6$ and $J = 6 - 5$) (Leurini et al. 2015).

Second, as discussed in Liseau et al. (2006), to match well the model-predicted and observed intensity-ratio of [OI] $63 \mu\text{m}/[\text{OI}] 145 \mu\text{m}$, one has to resort to either extremely high optical depths ($A_{\text{V}} > 100 \text{ mag}$) or take into account the absorption from the source cloud itself or/and the clouds along the line of sight. With the spectrally-resolved [OI] $63 \mu\text{m}$ line enabled by SOFIA/GREAT (Heyminck et al. 2012), it has indeed been observed in G5.89 – 0.39 that the emission of [OI] $63 \mu\text{m}$ is severely contaminated by self-absorption and absorption by clouds along the line of sight (Leurini et al. 2015). Although observational evidence is still scarce at the moment of writing, we judge it best to exclude [C I] $158 \mu\text{m}$ and [OI] $63 \mu\text{m}$ when searching for the best physical parameters. As to the [OI] $145 \mu\text{m}$ emission, since the observation of this transition covers only a small portion ($\sim 20\%$) of the FOV, we opt to exclude this line as a direct constraint to the models for the consistency. However, a good comparison between the model-predicted and observed

line intensities of [OI] $145 \mu\text{m}$, wherever it is possible, is ensured in our final results.

Third, in order to properly simulate the ^{13}CO emissions, one has to consider the chemical effects due to mutual shielding by its isotopologue, ^{12}CO . Theoretical computation has indicated that the ^{13}CO lines can be more efficiently shielded by ^{12}CO than by itself (Visser et al. 2009). The Meudon PDR code is capable of simulating this process by solving the exact radiative transfer as described in Goicoechea & Le Bourlot (2007). However, this heavy computation would cost days in order to successfully simulate one model, *i.e.* one combination of P , G_{UV} and A_{V} . To efficiently produce the entire model-grid required for the analysis, we adopt the FGK approximation (Federman et al. 1979) that takes only self-shieldings into account. This simplification would result in the underestimate of ^{13}CO line intensities. Therefore they are excluded from constraining the best physical parameters.

Prior to the search of best physical parameters on a given pixel based on the non-uniform grid of 1367 PDR models described above, we construct a numerical function that linearly interpolates the grid between its main free parameters, P , G_{UV} and A_{V} , to convert the grid into a continuous 3-dimensional grid-function. We use radial-basis-functions (`scipy.interpolate.Rbf`) to produce the grid-function, $M(P, G_{\text{UV}}, A_{\text{V}})$. In addition to the three free parameters, P , G_{UV} , and A_{V} , an additional free parameter, named scaling factor (ϕ) is introduced to describe several points. First, this parameter contains the information about the ratio of angular sizes of the observed clouds and beam, *i.e.* $\phi = \Omega_{\text{cl}}/\Omega_{\text{beam}}$, where Ω_{cl} is the physical angular size of observed CO clouds and Ω_{beam} is the beam area. Second, it also contains the information about the inclination angle of PDR components in the FOV with the line-of-sight. The Carina I-E region is known to host an edge-on PDR (Brooks et al. 2003), but all detected CO emission in our FOV may not come from edge-on PDRs. So we use face-on line intensities in our grid of PDR models and scale them with ϕ to consider limb-brightening effect. Third, this parameter also accounts for the possibility that several PDR components are superposed along the line of sight. At each pixel, we search for the combination of ϕ , P , G_{UV} , and A_{V} , that best matches the observed ^{12}CO line intensities by minimizing a normalized χ^2 :

$$\chi^2 = \sum_{i=1}^{N_{\text{obs}}} \frac{1}{(N_{\text{obs}} - N_{\text{p}} - 1)} \frac{[I_i - \phi M_i(P, G_{\text{UV}}, A_{\text{V}})]^2}{\sigma_i^2}. \quad (1)$$

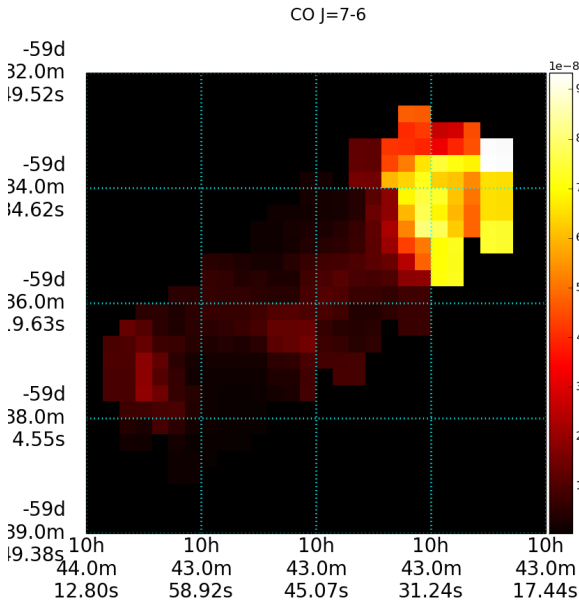


Fig. 4: Integrated intensities of CO $J = 7 - 6$ from our FOV. The displayed color-scale is in units of $\text{W m}^{-2} \text{sr}^{-1}$.

In Equation (1), N_{obs} and N_p represent the available numbers of the observed CO and C lines and the free parameters ($N_p = 4$), and I_i , σ_i , and $M_i(P, G_{\text{UV}}, A_V)$ denote the observed line intensity, its uncertainty, and the simulated line-intensity for the i -th transition.

As the S/N -ratio of the observed CO transitions generally decreases from CO $J = 11 - 10$ to CO $J = 12 - 11$ and to CO $J = 13 - 12$, we rule out the possibility that the intensities for high- J CO transitions beyond the bandwidth of *Herschel* SPIRE/FTS would be higher than the observed CO $J = 13 - 12$ transitions. An artificial penalty in the minimization procedure is forced to better constrain the best-fit solutions. When calculating χ^2 , a penalty is assigned to a given model that predicts $I(\text{CO } J = 13 - 12) > I(\text{CO } J = 12 - 11)$ and $I(\text{CO } J = 12 - 11) > I(\text{CO } J = 11 - 10)$.

We adopt the limited-memory BFGS (L-BFGS) algorithm in our minimization procedure (`scipy.optimize.minimize`) to search for the local minimum in the χ^2 -space. To ensure that the returned solution of $(\phi, P, G_{\text{UV}}, A_V)$ indeed corresponds to the global minimum in the χ^2 -space, we randomly choose 100 sets of initial free parameters and output all the solutions found by `scipy.optimize.minimize`. For a given pixel, the solution that corresponds to minimum χ^2 is chosen to be the final solution. The uncertainties for the constrained solutions are then estimated with 300 Monte-Carlo experiments with an assumption of Gaussian distributions for the uncertainties of the integrated line-intensity for each transition.

4. Results

4.1. CI and CO emission

The CO emission is observed from $J = 4 - 3$ to $J = 13 - 12$, along with [C I] $370 \mu\text{m}$ and [C I] $609 \mu\text{m}$ across the whole FOV (see figures in the Appendix). In the Car I-E region at the northwest, the intensities of the CO and [C I] lines are generally higher by one order of magnitude than those observed in Car I-S and Car I/II. Beyond $J = 10 - 9$, the emission is concen-

trated in the Car I-E and locally in the Car I/II regions. To get a global view on the spatial distribution of the CO excitation over the FOV, we first approximate the excitation temperature (T_{ex}) of CO transitions observed by the *Herschel* SPIRE/FTS under the LTE assumption. The reduced- χ^2 for fitting each observed CO SLED with LTE is between 0.5 and 2.5, with an average value of ~ 1.5 throughout the FOV. In the Car I-E region, the T_{ex} values are between 70 and 100 K. In the Car I-S region, the T_{ex} values are between 45 and 55 K. In the Car I/II region, the T_{ex} values are generally between 65 and 70 K, except a local (~ 0.5 pc in diameter) observation of $T_{\text{ex}} \sim 80$ K. The observed ratio of [C I] $370 \mu\text{m}$ /[C I] $609 \mu\text{m}$ is between 2.9 and 3.7 in the Car I-E region, corresponding to T_{ex} values between 33 and 41 K, which is consistent with the NANTEN2 observations (Kramer et al. 2008). In the Car I/II region, the observed ratio of [C I] $370 \mu\text{m}$ /[C I] $609 \mu\text{m}$ is around 2.5, corresponding to $T_{\text{ex}} \sim 28$ K. In the Car I-S region, the [C I] $370 \mu\text{m}$ and [C I] $609 \mu\text{m}$ are not detected above 3σ threshold. The observed spatial trends of the [C I] and CO excitation are generally consistent with each other, showing molecular gas of higher-excitation states in the Car I-E region.

As the sensitivity of the instrument is at the highest around the $J = 7 - 6$ transition (Table 2), we present an overview on the morphology of CO emission based on the CO $J = 7 - 6$ line intensity. Figure 4 shows the CO $J = 7 - 6$ line intensity distribution within our FOV. Comparing with the background optical image shown in Figure 2, the observed CO gas fills up most of the optically-thick region. The most prominent CO and C-emission is found in the Car I-E region, with an average value of $5.3 \times 10^{-8} \text{ W m}^{-2} \text{sr}^{-1}$ for the CO $J = 7 - 6$ intensity, and peaks at the northwest corner of the FOV with a value of $9.3 \times 10^{-8} \text{ W m}^{-2} \text{sr}^{-1}$. All 77 pixels ($\sim 2'$ or ~ 1.3 pc in diameter) covered in this region have observed CO $J = 7 - 6$ line intensities above 3σ threshold. This region sits at a projected distance of ~ 2.3 pc from Trumpler 14.

Moving to the Car I-S region, the area ($\sim 4'$ or ~ 2.5 pc in diameter) is mostly dominated by the H II region ionized by Trumpler 14. About 30% of the Car I-S region has no observed CO $J = 7 - 6$ emission at above 3σ threshold, while the CO emission observed at above 3σ is distributed along the dust-lane. One double-lined spectroscopic binary (SB2) system, *ALS 15 204* (O7.5Vz+O9: V), and a B0 star, *ALS 15 203*, which are identified as members of Trumpler 14 are found near the center of Car I-S (Apellániz et al. 2016). Along with other stellar members of Trumpler 14, these two stars can have important contribution to the excitation of CO gas in the region. The CO $J = 7 - 6$ emission detected in this region is the weakest within our FOV. Among the pixels with detected CO $J = 7 - 6$ emission ($> 3\sigma$), the average intensity is $7.6 \times 10^{-9} \text{ W m}^{-2} \text{sr}^{-1}$, which is about an order of magnitude fainter than that in Car I-E.

The Car I/II region at the southeast corner of our FOV is sitting at the intersection of two interstellar clouds, Car I and Car II, as defined by the radio thermal continuum observed at 5 and 0.843 GHz (Gardner & Morimoto 1968; Whiteoak 1994). About 70% of the Car I/II area has CO $J = 7 - 6$ emission detected at above the 3σ threshold, and the detected CO $J = 7 - 6$ emission has an average intensity of $9.8 \times 10^{-9} \text{ W m}^{-2} \text{sr}^{-1}$. This region sits right in the middle between the two most massive star-clusters of the Carina Nebula, Trumpler 14 and Trumpler 16, both of which can provide UV-photons for the observed CO emission.

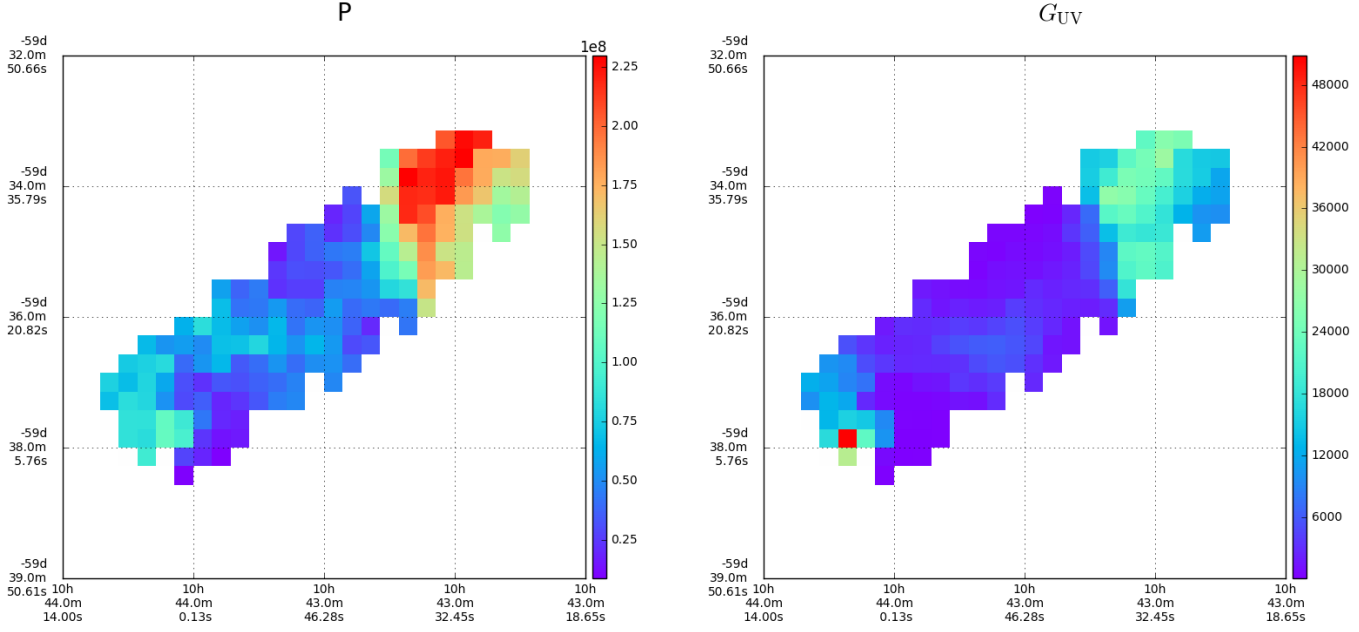


Fig. 5: Best physical parameters derived at each pixel from the comparison of observations with PDR models. On the left panel is shown the thermal pressure, P , in K cm^{-3} and on the right panel the FUV scaling factor, G_{UV} .

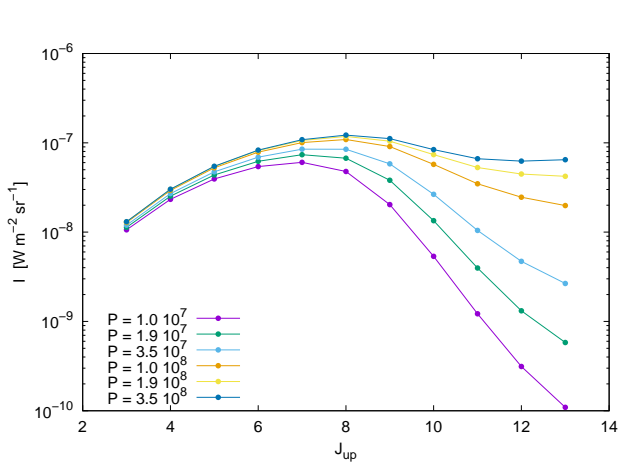


Fig. 6: CO SLEDs generated with the Meudon PDR code with G_{UV} and A_V fixed at 10^4 and 10 respectively and with different thermal pressures.

4.2. Physical conditions

We determine the physical conditions (P , G_{UV} , A_V and ϕ) at each pixel following the method described in section 3.2. CO mid- J and high- J lines are good tracers of the gas pressure as it can be seen on Figure 6 and we expect this parameter, as well as G_{UV} that controls the energy input and photo-destruction rates be well constrained. As only ^{12}CO lines with $J_{\text{up}} > 3$ and C lines, which probe only the surface layer of molecular gas are used in constraining the solutions, the total A_V parameter of our models is not reliably constrained. So, we do not discuss this parameter in the following.

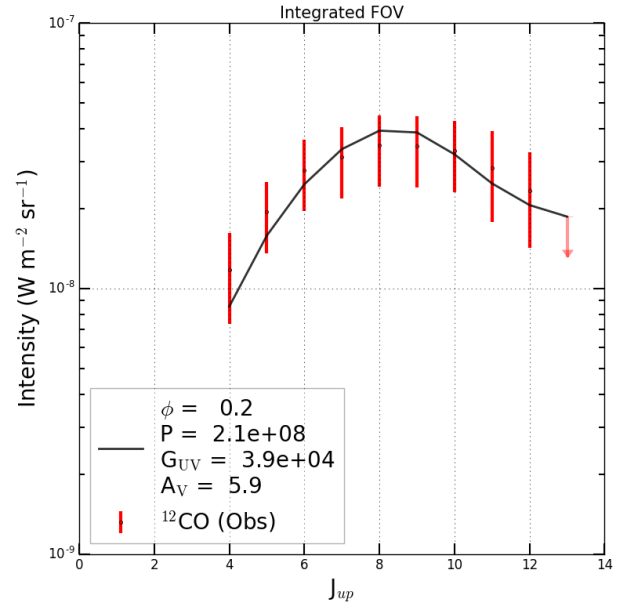


Fig. 7: CO SLED obtained by integration of the emission on the whole FOV (red bars). The black line represents the best PDR model in the grid of models that reproduces the observation.

A good agreement between PDR models and observed CO and [C I] line intensities is found at all pixels. To illustrate the general goodness of solutions, comparisons between the observed CO line intensities and those simulated by the Meudon PDR code are presented with the integration of CO lines on the whole FOV (Figure 7), and with three typical pixels from the Car I-E, Car I-S, and Car I/II regions (Figure 8). The reduced χ^2 values vary between 0.2 to 0.7 across the FOV. CO and [C I]

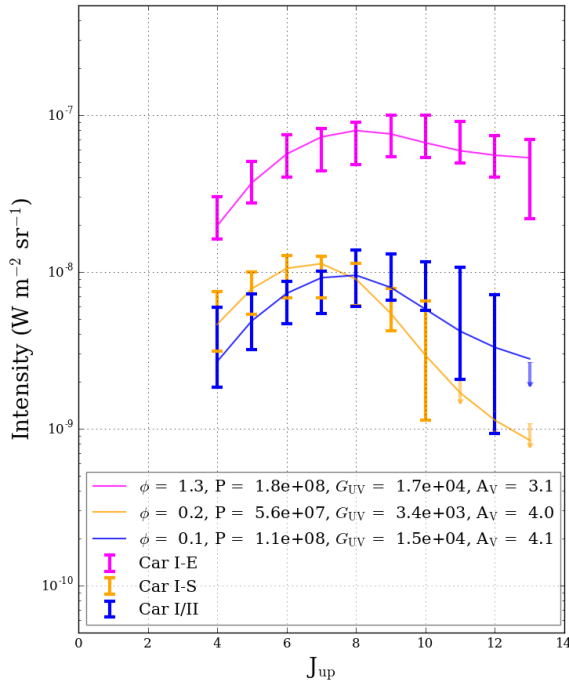


Fig. 8: CO SLEDs observed from the three yellow-masked pixels chosen from the Car I-E, Car I-S, and Car I/II regions as indicated in Figure 2. The best-fit Meudon PDR models are overplotted the solid lines.

line intensities predicted by the Meudon PDR models are generally consistent with the *Herschel* SPIRE/FTS observations. We also examine whether or not the observed intensities of ^{13}CO , [OI] 63 μm , [OI] 145 μm , and [CII] 158 μm computed by the PDR models but not used in the minimization procedure are consistent with the observations (see arguments in Section 3.2). As our constraints, the ^{12}CO and [CI] emissions may not probe the full optical-depth of the PDRs, we expect the model-predicted ^{13}CO intensities to be always lower than the observed values. In our observations, the ^{13}CO emission is only detected up to the $J = 8 - 7$ (from $J = 4 - 3$) transition in the Car I-E region, and marginally in the Car I-S and Car I/II regions. In this region, comparing the model-predicted and observed intensities of ^{13}CO transitions, the model-predicted values of ^{13}CO transitions generally represent $\sim 10\%$ of the observed intensities. Although the effects from mutual shielding of ^{12}CO may account partly for this under-estimation, further investigations would be needed in order to understand the observed ^{13}CO emission.

For the [CII] 158 μm emission, the ratio of model-predicted and observed intensities varies between 0.02 and 0.3. Within the Car I-E region, which is dominated by the PDRs, the observed [CII] 158 μm intensities are between 3 to 10 times larger than the model-predicted values. In Car I-S and Car I/II regions, where PDRs no longer dominate the FOV, the observed [CII] 158 μm intensities are about 10 to 50 times larger than the model-predicted values. Generally, this spatial trend is consistent with the results found in Oberst et al. (2011). As the [CII] 158 μm emission can also originate from ionized gas and neutral gas at more diffuse states than the modeled molecular gas based on the CO and [CI] observations, we expect under-estimated

[CII] 158 μm intensities from the models. By approximating the *ISO*-observed [CII] 158 μm emission as a linear combination of the [OI] 63 μm and [NII] 122 μm emissions, Mizutani et al. (2004) estimate that the contribution to the [CII] 158 μm emission by the ionized gas is about 20% in the Carina Nebula. Based on the *ISO*-observed ratio of [NII] 122 μm and [NII] 205 μm emissions, Oberst et al. (2011) estimate this contribution to be 37%. However, the direct association of the observed [OI] 63 μm emission to the PDRs is uncertain, and a large fraction of the [CII] 158 μm -emitting neutral gas may not be spatially associated to the denser CO-emitting cloud, as recently revealed in the Horsehead Nebula by the SOFIA/GREAT observations (Pabst et al. 2017). The adopted isobaric PDR models, which well describe the observed CO and [CI] emissions, may only account for a small fraction of the [CII] 158 μm emission originated from the PDRs. Without spectrally-resolved observations, as urged by the SOFIA/GREAT observations from N 159 of the Large Magellanic Cloud (LMC) (Okada et al. 2015), it is unattainable to pin down the [CII] 158 μm emission directly associated with the CO-emitting clouds.

For the [OI] 63 μm transition, as discussed in Section 3.2, the observed interstellar [OI] emission at 63 μm can suffer largely from foreground absorption (Liseau et al. 2006), which leads to the generally over-estimated [OI] 63 μm emission with PDR models. Within our FOV, the ratio of model-predicted and observed intensities is always larger than 10. The model-predicted [OI] 145 μm transitions, on the other hand, are generally reasonable, and the ratio of model-predicted and observed line intensities are between 1 and 3 over the FOV.

Figure 5 shows the maps of derived P and G_{UV} . As each pixel is modeled independently in the process, the smooth appearance on the P and G_{UV} maps reassures that our solutions are not strongly degenerated. Based on the solutions, Car I-E is dominated by high pressure gas ($P \sim 1.5 - 2.2 \times 10^8 \text{ K cm}^{-3}$) heated by strong UV radiation fields ($G_{\text{UV}} \sim 3 \times 10^4$). In the Car I-S region, lower P ($\leq 7 \times 10^7 \text{ K cm}^{-3}$) and G_{UV} ($3000 < G_{\text{UV}} < 1.2 \times 10^4$) values are found. The pressure and the intensity of the radiation field then slightly rise into the Car I/II region ($P \sim 10^8 \text{ K cm}^{-3}$ and $G_{\text{UV}} \sim 10^4$). The ϕ parameter found by our procedure varies between 0.2 and 1.4 in the FOV. The higher values are found in the Car I-E region. Since in our procedure we use face-on values for simulated line intensities, this is consistent with a PDR seen edge-on that fills the beam as mentioned by previous authors (Brooks et al. 2003; Kramer et al. 2008). The lower values are found in the Car I-S area, consistent with a region where molecular gas fills up the beam partially.

The G_{UV} values obtained by our comparison between PDR models and observations are larger than the ones cited in previous works. In particular Brooks et al. (2003) estimated the FUV flux in several ways. First, based on the Kaufman et al. (1999) PDR models, they find a FUV scaling factor between 600 and 10^4 in the Habing unit. They also considered the most massive stars in the Tr 14 cluster and estimated the resulting flux at the [CII] peak location (10:43:22 -59:34:45), finding 1.4×10^4 in the Habing unit, *i.e.* 10^4 in the Mathis units.

We re-investigate the FUV luminosity that illuminates the molecular gas observed in the FOV. The spatial variation of our derived G_{UV} across the FOV suggests that the CO clouds may be distributed at different distances from the illuminating stars. As the massive stellar members of Trumpler 14 and 16 are well identified (Vazquez et al. 1996; Sana et al. 2010; Hur et al. 2012; Sota et al. 2014; Apellániz et al. 2016; Alexander et al. 2016), we are able to compare the derived G_{UV} with the estimated UV-photons input by the nearby OB-stars.

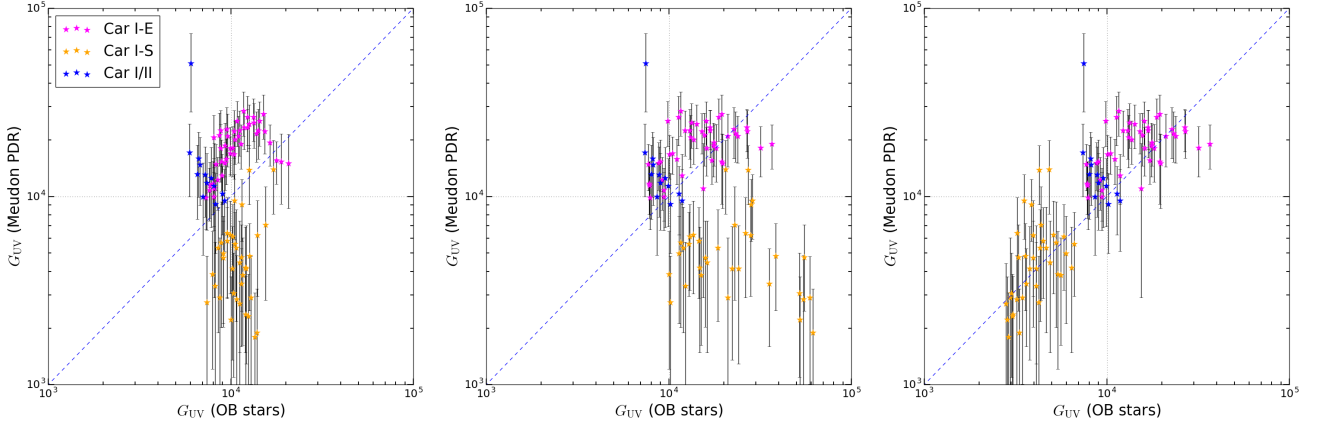


Fig. 9: Comparison of the G_{UV} values obtained with the Meudon PDR code and the values evaluated from the stellar composition within our FOV. Only pixels with good ($S/N > 3$) detection of CO $J = 7 - 6$ are plotted. The dashed lines indicates a 1 : 1 relationship between the quantities on the axes. The uncertainties of the G_{UV} values derived with the Meudon PDR models are estimated with the MC experiment as discussed in Section 3.2. *Left*: All OB-stars are assumed to be at the center of their host star-clusters, *i.e.*, Trumpler 14 and 16. The observed CO gas is assumed to lie on the plane perpendicular to the line of sight at a 2.35 kpc distance. *Center*: The distribution of OB-stars is considered coplanar at their observed (α, δ) coordinates. The geometry of the CO gas is assumed to be coplanar as in the left panel. *Right*: The distribution of OB-stars is considered coplanar at their observed (α, δ) coordinates. The geometry of the CO gas is assumed as the shape indicated in Figure 11.

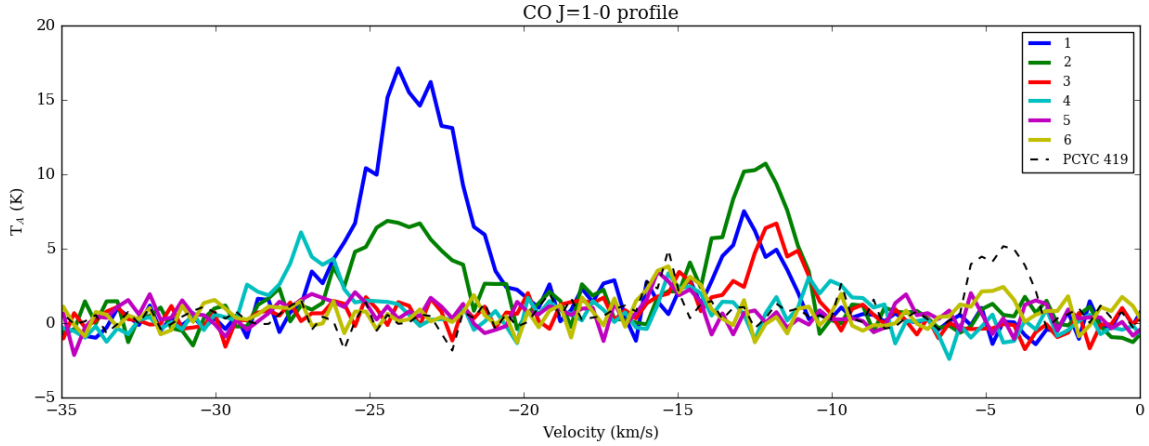


Fig. 10: Spectrally-resolved line profiles at six positions indicated in Figure 2. The data is taken as a part of the Carina Parkes-ATCA Radio Continuum Survey (Rebolledo et al. 2016). The dashed line indicates the line profile at a ~ 0.2 pc region from Car I/II (see Section 5.1).

Table 5 lists all observed OB-stars within a projected distance of 7 pc ($\sim 7.5'$) from the center of our FOV with updated FUV luminosity. If one is unaware of the spatial distributions of stars and naively assumes that all the listed stars are located at the center of their host star-clusters, and that the observed CO gas lies at the same plane perpendicular to our line of sight at a 2.3 kpc distance, the estimated stellar G_{UV} values and the G_{UV} values derived from the Meudon PDR models agree poorly with each other (left panel in Figure 9). However, when the sky coordinates of the nearby OB-stars are taken into account (still coplanar with the CO gas), the comparison between the estimated stellar G_{UV} values and the G_{UV} values derived from the Meudon PDR models slightly improves in the Car I-E and Car I/II regions (center panel in Figure 9).

Two stellar members of Trumpler 14, an O-stars binary system, *ALS 15 204*, and a B0 star, *ALS 15 203*, are observed in the Car I-S region (near the pointing #3 in Figure 2). Observations with the 4m Anglo-Australian Telescope (AAT) have sug-

gested that a separate subcluster may be formed around these two stars (Alexander et al. 2016). Judging from the spectrally-resolved CO $J = 1 - 0$ observations⁷ (Rebolledo et al. 2016) across the six central pointings (see Figure 2) from our FOV in Figure 10, the CO $1 - 0$ emission at Car I-S region is dominated by the velocity component at around -13 km s^{-1} (pointings #3, #4, and #5). Assuming that the subcluster carves out a cavity of CO gas in the Car I-S region, the observed CO emission from the region may be associated to the cloud sitting further away from the observer along the line of sight. With a simple cloud geometry demonstrated in Figure 11, which is created by moving the cloud directly over *ALS 15 204* and *ALS 15 203* in

⁷ Taken from the Carina Parkes-ATCA Radio Continuum Survey publicly available at <http://mopra.org/data/>

Table 5: A list of massive stars found within a projected distance of 7 pc from the center of FOV (10 : 43 : 45.07, −59 : 36 : 19.63).

Name	RA (J2000)	Dec (J2000)	Stellar type	T (10 ³ K)	L_{FUV} (10 ⁵ L _⊙)	Binary
HDE 303312	10 : 43 : 30.842	−59 : 29 : 23.8	O9.7 IV	29.5 ^a	0.31 ^a	VB:0-1 SBE
ALS 15204	10 : 43 : 41.237	−59 : 35 : 48.18	O7.5 V	35.88	1.50	VB:1-3 SB2?
CPD -58 2611	10 : 43 : 46.695	−59 : 32 : 54.82	O6 V	38.87	2.13	VB:1-2 SB1?
ALS 15207	10 : 43 : 48.707	−59 : 33 : 24.1	O9 V	32.88	1.03	VB:0-1
HD 93128	10 : 43 : 54.372	−59 : 32 : 57.37	O3.5 V	43.86	3.63	VB:3-22
Trumpler 14-9	10 : 43 : 55.354	−59 : 32 : 48.61	O8.5 V	33.88	1.17	VB:many
HD 93129 AaAb	10 : 43 : 57.462	−59 : 32 : 51.27	O2 I	43.90	4.85	VB:many
HD 93129 B	10 : 43 : 57.638	−59 : 32 : 53.5	O3.5 V	43.86	3.63	VB:many
CPD -58 2620	10 : 43 : 59.917	−59 : 32 : 25.36	O7 V	36.87	1.70	VB:1-6
ALS 15206	10 : 44 : 00.927	−59 : 35 : 45.74	O9.2 V	32.48	0.98	VB:0-2
CPD -58 2627	10 : 44 : 02.445	−59 : 29 : 36.77	O9.5 V	31.89	0.90	VB:1-2
HD 93160	10 : 44 : 07.267	−59 : 34 : 30.61	O7 III	36.08	0.70	VB:1-2
HD 93161 A	10 : 44 : 08.84	−59 : 34 : 34.49	O7.5 V	35.88	1.50	VB:1-2 SB2
HD 93161 B	10 : 44 : 09.08	−59 : 34 : 35.3	O6.5 IV	37.93 ^b	1.40 ^b	VB:1-3 SB1?
HD 93162	10 : 44 : 10.389	−59 : 43 : 11.09	O2.5 If*/WN6	42.96 ^c	4.67 ^c	VB:1 SB2
ALS 15210	10 : 44 : 13.199	−59 : 43 : 10.33	O3.5 I	41.08	4.30	VB:2
HDE 303311	10 : 44 : 37.463	−59 : 32 : 55.44	O6 V	38.87	2.13	VB:1
Tr 14-30	10 : 43 : 33.35	−59 : 35 : 11.1	B1 Ia	26.00 ^a	0.40 ^a	–
ALS 15203	10 : 43 : 41.21	−59 : 35 : 53.3	B0 V	31.50	0.26	–
Tr 14-28	10 : 43 : 43.56	−59 : 34 : 03.5	B2 V	20.60	0.01	–
Tr 14-22	10 : 43 : 48.81	−59 : 33 : 35.2	B2 V	20.60	0.01	–
Tr 14-24	10 : 43 : 50.9	−59 : 33 : 50.6	B1 V	26.00	0.08	–
Tr 14-18	10 : 43 : 57.96	−59 : 33 : 53.7	B1.5 V	24.50	0.05	–
Tr 14-19	10 : 43 : 58.46	−59 : 33 : 01.6	B1 V	26.00	0.08	–
Tr 14-29	10 : 44 : 05.11	−59 : 33 : 41.47	B1.5 V	24.50	0.05	ERO 21
Tr 16-124	10 : 44 : 05.83	−59 : 35 : 11.7	B1 V	26.00	0.08	–
Tr 16-245	10 : 44 : 13.8	−59 : 42 : 57.1	B0 V	31.50	0.26	SB2
Tr 16-246	10 : 44 : 14.75	−59 : 42 : 51.8	B0.5 V	29.00	0.18	–
Tr 16-11	10 : 44 : 22.52	−59 : 39 : 25.8	B1.5 V	24.50	0.05	–
LS 1840	10 : 44 : 24.62	−59 : 30 : 35.9	B1 V?	26.00	0.08	SB2
Tr 16-122	10 : 44 : 25.49	−59 : 33 : 09.3	B1.5 V	24.50	0.05	–
Tr 16-94	10 : 44 : 26.47	−59 : 41 : 02.9	B1.5 V	24.50	0.05	–
Tr 16-18	10 : 44 : 28.97	−59 : 42 : 34.3	B2 V	20.60	0.01	–
Tr 16-12	10 : 44 : 29.42	−59 : 38 : 38.1	B1 V	26.00	0.08	–
Tr 16-10	10 : 44 : 30.37	−59 : 37 : 26.7	B0 V	31.50	0.26	SB2
Tr 16-17	10 : 44 : 30.49	−59 : 41 : 40.6	B1 V	26.00	0.08	–
Tr 16-13	10 : 44 : 32.9	−59 : 40 : 26.1	B1 V	26.00	0.08	–
Tr 16-14	10 : 44 : 37.19	−59 : 40 : 01.5	B0.5 V	29.00	0.18	–
Tr 16-16	10 : 44 : 40.31	−59 : 41 : 49	B1 V	26.00	0.08	–

Notes. For O stars, the luminosity and effective temperature (T_{eff}) are calculated based on the calibration of solar-metallicity O stars of type I, III, and V (Martins et al. 2005). The calibration for B stars are based on Pecaut & Mamajek (2013).

^(a) from Povich et al. (2011) ^(b) from Gagné et al. (2011) ^(c) The listed luminosity for HD 93 162 is calculated as if it is an O 2.5 I star. However, the luminosity for this star is uncertain and can possibly be five times brighter (Hamann et al. 2006).

Car I-S further by $\sim 3 \text{ pc}^8$, ensuring the spatial continuity of the cloud along constant slopes into Car I-E and Car I/II, and taking the coordinates of nearby OB-stars into account, the G_{UV} values derived with the Meudon PDR code come to an excellent agreement with the expected G_{UV} contributed by the OB-stars in the field without scaling (right panel in Figure 9). Even if we assume that the distance to Trumpler 14 is $\sim 2.9 \text{ kpc}$ (Hur et al. 2012), in which case the expected G_{UV} contributed by the OB-stars would decrease by a factor of ~ 1.5 , the agreement still holds within the estimated uncertainties.

In our simple and crude geometry assumption, all the stars in the vicinity are located on the same plane, which is unlikely the reality. Unfortunately, given the uncertainties in our observations and models, we do not have sufficient information to accurately

constrain the positions of stars and clouds along our line of sight. However, the excellent agreement displayed in Figure 9 demonstrates that our simple assumption may be a good approximation to the reality.

5. Discussion

5.1. UV radiation field in Carina

The CO emitting gas observed in this work only cover a small area ($\sim 2 \times 5 \text{ pc}^2$) of the Carina Nebula (Figure 1). In this subsection, we discuss our findings under the frame of the whole Carina Nebula. The Carina Nebula is famous for its bipolar structure with its major axis almost perpendicular to the Galactic plane. In its northern part, expansion along the Galactic plane caused by the formation of young star clusters is inhibited by the dense molecular gas (Smith et al. 2000). One of the biggest mysteries in the Carina Nebula is its supernova history.

⁸ This distance is motivated by the assumption that the cavity created by the subcluster has a similar dimension along the line of sight as the approximate size of the Car I-S region.

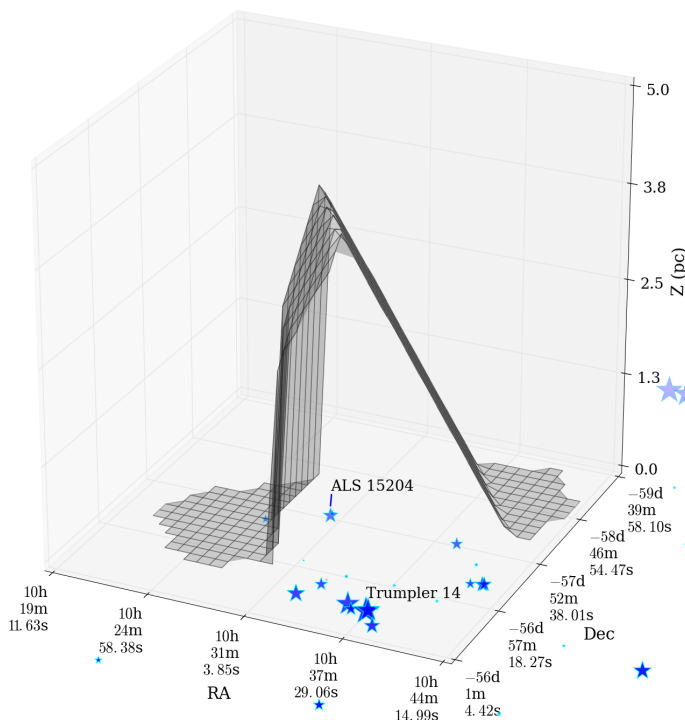


Fig. 11: In this figure, the gray mesh demonstrates the estimated 3D cloud structure in this work. The blue star symbols indicate the OB-stars in the FOV with their sizes in proportion to the FUV luminosities of stars. The Z-axis indicates the offset along the line of sight where $Z = 0.0$ is at 2.3 kpc from us. Stars that are outside the FOV (Figure 2) toward the south are displayed in fainter colors.

Based on the observed line-splitting of ionized gas and the total gas mass estimated from the cool dust mass, Smith & Brooks (2007) estimated the total kinetic energy of the nebula to be 8×10^{51} erg, which represents 30% of the total mechanical energy input by the stellar wind during the past 3 Myr (Smith 2006a). The lack of radio or X-ray synchrotron emission indicates that a recent supernova activity is unlikely.

However, confirmation of the diffuse X-ray emission which offsets from the young massive star clusters and the discovery of an isolated neutron star, 2XMM J104608.7 – 594306, have led to a possible supernova history in the Carina Nebula (Townsend et al. 2011; Pires et al. 2015). In the vicinity of our FOV, an observed B-type star (Tr 14-29 in Table 5) is moving with a high velocity ($\sim 100 \text{ km s}^{-1}$) toward the center of Trumpler 14, directly away from 2XMM J104608.7 – 594306. If Tr 14-29 is the runaway star associated with 2XMM J104608.7 – 594306 during a past supernova explosion, its estimated flight time is $\sim (1.1 - 3) \times 10^4$ yr, which is roughly consistent with the absence of a supernova remnant in the Carina Nebula (Ngoumou et al. 2013). All these characteristics suggest that the region in our FOV may be associated with a Galactic superbubble. The observed physical conditions of PDRs can thus provide a suitable analogue for the observations of more faraway starburst regions hosted in similar interstellar environments, such as the famous 30 Doradus.

Comparing the CO SLEDs from the Car I-E, Car I-S, and Car I/II regions (see Figure 8), it is clear that the Car I-E region is dominated by CO gas of high thermal pressure and strong radiation fields ($P = 1.8 \times 10^8 \text{ K cm}^{-3}$ and $G_{\text{UV}} = 1.7 \times 10^4$). The thermal pressure and the strength of radiation

decrease ($P = 5.6 \times 10^7 \text{ K cm}^{-3}$ and $G_{\text{UV}} = 3.4 \times 10^3$) in the Car I-S region and then increase again in the Car I/II region ($P = 1.1 \times 10^8 \text{ K cm}^{-3}$ and $G_{\text{UV}} = 1.5 \times 10^4$). Within our FOV, the PDRs in the Car I-E region have been previously studied by several groups. Based on the approximate stellar composition and the far-infrared (FIR) continuum observed in Car I, Brooks et al. (2003) and Mizutani et al. (2004) have estimated the G_{UV} to be $\sim 10^4$ in the Habing unit. On the other hand, estimations with PDR models have been thus far giving somehow lower G_{UV} values. Constrained by the $[\text{CII}] 158 \mu\text{m}$, $[\text{OI}] 63$ and $[\text{OI}] 145 \mu\text{m}$ emissions observed with *ISO*, the interpretations with the PDR Toolbox (Pound & Wolfire 2008; Kaufman et al. 2006) estimate the G_{UV} values to be around 1390, in the Habing unit (~ 1000 in the Mathis unit), in Car I (Oberst et al. 2011). With a clumpy PDR model, using the observed CO $J = 2 - 1$, $J = 4 - 3$, $J = 7 - 6$, and the two atomic carbon lines, $[\text{C}] 370$ and $609 \mu\text{m}$, the strength of the radiation field in Car I-E is estimated to be ~ 3200 in the Habing unit (~ 2500 in the Mathis unit) (Kramer et al. 2008). In a big picture, these results indicate that the UV-photons and stellar winds provided by nearby massive stars are more than sufficient in supporting the global heating of CO and $[\text{C}]$ emissions observed in this region.

Using the Meudon PDR models, the G_{UV} values constrained from the *Herschel* SPIRE/FTS observations in the Car I-E region range between 10^4 and 3×10^4 , which are generally higher than the values found in the literature. However, the excellent agreement of the model-derived G_{UV} values with the estimated radiation fields from the nearby stellar composition appears throughout our FOV, as demonstrated in Figure 9. Our analysis has confirmed that the chief energy source for the observed CO emissions is the UV-photons input by the massive stars in the vicinity. We would like to note from our results that in the Car I-E region, the model-derived G_{UV} values tend to be marginally higher than the G_{UV} contributed solely by the OB-stars. The emission of CO observed along the ionization front may also be supported by local heating sources. In Car I-E, narrow-band imaging-observations from the optical to the mid-infrared have revealed that many massive (B4 to A0) young stellar objects (YSOs) are distributed on or just behind the ionization front (Tapia et al. 2006). Along the ionization front, the model-derived thermal pressure values are the highest in our FOV ($\sim 2 \times 10^8 \text{ km cm}^{-3}$, see Figure 5). Interestingly, along the high-pressure ionization front, at the very edge of our FOV in the northwest, the highest values for the CO and $[\text{C}]$ emissions are observed (see figures in the Appendix). At this location (10:43:23.25, -59:33:56.9), a massive class I YSO, V723 Car, has been observed to go into outburst just before 2003 (Tapia et al. 2015). All ^{12}CO transitions covered by the *Herschel* SPIRE/FTS and ^{13}CO , up to $J = 8 - 7$, is unambiguously detected here. This result suggests a potential contribution of local heating sources. Unfortunately, we cannot derive the physical conditions from this location due to the variation of instrument resolution, but it will be an interesting target for future high-resolution observation for understanding the interplay between the formation of massive YSOs and their host environment.

The location of Car I/II region has almost the same distances to the centers of Trumpler 14 and 16 and lies at the intersection of Car I and Car II. Based on the projected distances from the O- and B-stars in the vicinity (see Table 5), the G_{UV} -values at the Car I/II region should be comparable or weaker than the Car I-E region. This is the case for most of the pixels in the region. Globally in Car I/II, the dust mass and temperature, derived from the photometry data in our FOV, are quite low, however CO is unambiguously observed (Wu et al. in prep.). This result is in

agreement with the comparison of dust-mass, estimated with the continuum at 1.2 mm (9 M_{\odot} , Brooks et al. 2005), and gas-mass, estimated with CO $J = 2 - 1$ (91 M_{\odot} (LTE) or 411 M_{\odot} (virial), Rathborne et al. 2002). The large discrepancy between the gas-mass estimated under LTE and virial assumption implies that the observed cloud is not gravitationally bound but supported by external radiation fields (Rathborne et al. 2002).

One thing that has been puzzling from our results is the local high G_{UV} values ($\sim 5 \times 10^4$) derived in the Car I/II region of our FOV (see Figure 5). At this location (10:44:03.89, -59:37:57.63), CO emission is well detected up to $J = 12 - 11$. Under the LTE assumption, the T_{ex} value derived locally is ~ 80 K, while T_{ex} is generally below 70 K in the Car I/II region. This point also appears as the only outlier in Figure 9, hinting that the UV-photons from nearby OB-stars may not be able to support the CO excitation. Observations in CO $J = 1 - 0$ with *Mopra* show a velocity component centered at -5 km s^{-1} , which appears only at this point in our FOV (see dashed-line in Figure 10), implying that the structure of CO gas may differ locally. The CO cloud observed here is likely heated partially by stellar members in Trumpler 14 and partially by the two nearby early-type stars, *HD 93 162* and *ALS 15 210*, of Trumpler 16. *ALS 15 210* has been classified as an O3.5 I star. The Wolf-Rayet star, *HD 93 162*, also known as *WR 25*, is possibly the most luminous known star in our Galaxy (up to $L = 6.3 \times 10^6 L_{\odot}$, Hamann et al. 2006), but it is still not sufficient to account for the local high G_{UV} value. The UV-photons input by the nearby massive stars simply cannot explain the model-derived G_{UV} values locally. Based on the modeling results of the $1 - 24 \mu\text{m}$ spectral energy distribution in the Carina Nebula, a type 0/I YSO of intermediate-mass with hard X-ray signature has been detected at (10:44:03.086, -59:37:48.41) (Povich et al. 2011) and listed in the Pan-Carina Young Stellar Object Catalog (PCYC) as *PCYC 419*. However, at the physical scale of $\sim 0.2 \text{ pc}$, we do not expect the outflow from an intermediate-mass YSO to dominate the heating of CO gas. To further understand the local heating mechanisms for the observed CO gas, high-resolution observations from the region is necessary.

5.2. CO at PDR interfaces

For more than 30 years, PDRs have been studied to understand the transition between atomic and molecular gas as well as the impact of the radiative feedback of massive stars on their parent cloud (Tielens & Hollenbach 1985; Sternberg & Dalgarno 1989). Before *Herschel* observations, the most accessible lines probing the very edge of PDRs and the physics and chemistry that take place in these interfaces were the atomic lines of O, C^+ and C as well as molecular lines of H_2 and a few CO lines. Comparisons of these observations to PDR models lead to the conclusion that the edge of PDRs can be seen as a clumpy medium in which dense clumps are embedded in a more diffuse medium (Stutzki & Guesten 1990; Parmar et al. 1991; Meixner & Tielens 1993; Tauber et al. 1994; Hogerheijde et al. 1995; Andree-Labsch et al. 2017). In this scenario, UV photons can penetrate deeply into the cloud through the interclump medium ($n_{\text{H}} \sim 10^4 - 10^5 \text{ cm}^{-3}$) and heat the edge of the dense clumps ($n_{\text{H}} \sim 10^6 - 10^7 \text{ cm}^{-3}$) where H_2 vibrational lines and CO mid and high-J lines are produced. More recently, *Herschel* observations of CO rotational emission in protostars, PDRs and extragalactic regions also showed high-J excitation. Shapes of CO SLEDs in different environments have been compared by Indriolo et al. (2017). In protostellar systems as Orion KL, the very high-J excitation ($J_{\text{up}} \sim 40$), indicates energy inputs through outflows and shocks (Goicoechea et al.

2015). In extragalactic regions, the sources of energy responsible for CO excitation are less clear because of the mixture of several emitting sources in the beam. Rosenberg et al. (2015) suggest that CO excitation in some Class I galaxies may be dominated by UV heating whereas Class III galaxies would require mechanical heating (shocks and turbulence) or X-rays heating.

Here, we find that highly illuminated ($G_{UV} \sim 10^4$) PDR models with high thermal pressures ($P \sim 10^8 \text{ K cm}^{-3}$) can successfully explain CO excitation in the Carina Nebula without introducing a clumpy cloud-structure. UV photons, via the photoelectric effect on grains, are the main heating mechanism. Isobaric models have been proposed as an alternative to the classical clump approach for the Orion Bar (Marconi et al. 1998; Allers et al. 2005). An isobaric model is found to successfully explain the CH^+ emission in the Orion Bar (Nagy et al. 2013). More recently, it is suggested that the PDRs can support several tens of atomic and molecular lines including H_2 lines and CO lines from $J = 4 - 3$ to $J = 23 - 22$ in two prototypical PDRs, the Orion Bar and NGC 7023 NW (Joblin et al. in prep.).

It is suggested that hot chemistry takes place at the edge of PDRs and is responsible for the mid-J and high-J CO lines that are observed (Joblin et al. in prep.). In our models, we simulate the formation of H_2 with the formalism described in Le Bourlot et al. (2012) that considers the Langmuir-Hinshelwood and Eley-Rideal mechanisms. This detailed treatment increases the formation rate of H_2 compared to the classical value determined in diffuse interstellar gas by Copernicus and FUSE, $3 \times 10^{17} \text{ cm}^3 \text{ s}^{-1}$ (Jura 1974; Gry et al. 2002) that is often used in astrochemical models. Typically, in the Car I-E area, we find a 3 to 4 times higher formation rate at the edge of the PDR. This enhanced formation rate allows H_2 to form close to the edge of the PDR, in warm gas (a few hundred Kelvins depending on physical conditions). In this warm gas, some key chemical reactions with H_2 usually inhibited because of large activation energies can be efficient because of, first, the relative velocity between the reactants and, second, the internal energy stocked in H_2 ro-vibrational levels. That is the case of the $\text{C}^+ + \text{H}_2$ reaction that forms CH^+ with an activation energy of 4537 K. We compute the rate of this reaction with the formalism of Agúndez et al. (2010).

Then, several chemical routes that start with CH^+ lead to the formation of CO. As a consequence, in bright PDRs, the formation of CO starts as soon as H_2 self-shielding becomes in effect. Figure 12 presents the density profiles of H, H_2 , C^+ , C and CO (total and in its levels $J = 4, 8$ and 13) as a function of A_V for a model with $P = 3.5 \times 10^8 \text{ K cm}^{-3}$ and $G_{UV} = 2 \times 10^4$. CO level $J = 13$ is populated before the C/CO transition. So, a fraction of the emission of CO in mid-J and high-J levels comes from a slab of the PDR in front of the C/CO transition. Recent *ALMA* observations of the Orion Bar presented in Goicoechea et al. (2016); Goicoechea et al. (2017) show the same trend of chemical stratification. In particular, SH^+ emission whose formation path is similar to the one of CH^+ but with an activation energy threshold of 9860 K, shows a clear front close to the edge of Bar.

5.3. P - G_{UV} relation

Figure 13 presents the thermal pressure as a function of G_{UV} for all the pixels of our Carina FOV. As the pressure, P , is derived from CO and C lines in this work, it is generally associated with neutral gas. Except in the Car I-S region, which is not very bright in the CO emission and dominated by the HII region, we fit a power-law relationship between P and G_{UV} values in Figure 13. In the Car I/II region, some pixels seem to have the same

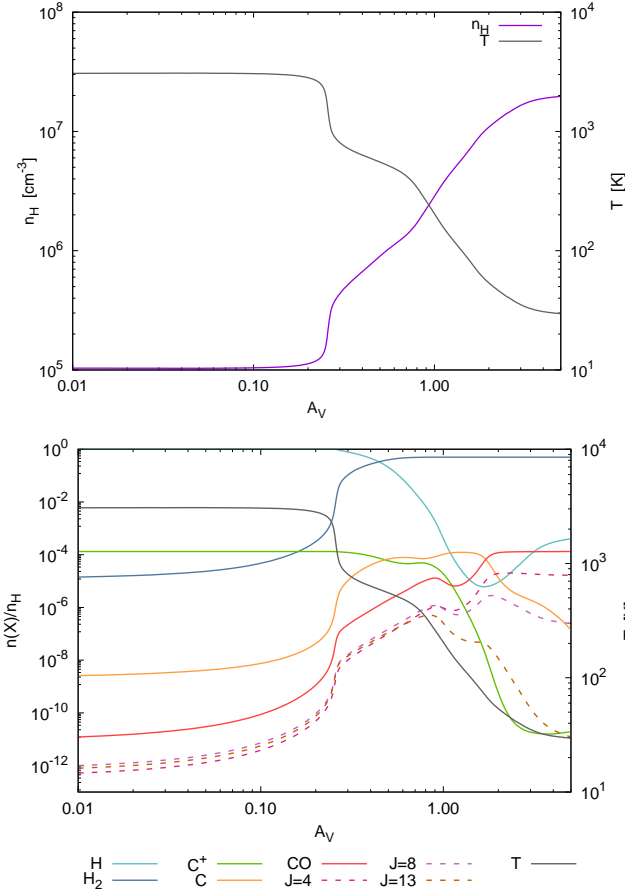


Fig. 12: Example of density and temperature profiles computed by the Meudon PDR code for a model with $P = 3.5 \times 10^8 \text{ K cm}^{-3}$, $G_{UV} = 2 \times 10^4$ and with a total depth $A_V = 10$. Top panel presents the proton density and the gas temperature profiles. Bottom panel presents the relative densities of H, H₂, C⁺, C and CO as well as the relative densities of CO J = 4, 8 and 13.

thermal pressure for different G_{UV} while for other ones P increases with G_{UV} . In the Car I-E region, which is dominated by the bright PDR, the relationship is the most prominent. From our observations, the empirical relationship between P and G_{UV} is:

$$P = 2.1 \times 10^4 G_{UV}^{0.9}. \quad (2)$$

In the extragalactic observation, a similar relationship has been suggested in Wu et al. (2015). In the Galactic PDRs, a similar relationship between P and G_{UV} values spanning over more than 3 orders of magnitude has also been observed (Joblin et al. in prep.). The observed relationship suggests that the UV radiation field of massive stars may create a high pressure layer at the edge of PDRs and the physical mechanism at play could be the UV induced photo-evaporation as described in Bertoldi (1989); Bertoldi & Draine (1996). As the Meudon PDR model describes a stationary system, a hydrodynamical PDR code is required to understand the exact mechanism leading to the compression of the gas and to quantify its effect (Bron et al. in prep.).

6. Conclusion

The *Herschel* SPIRE FTS uses a pioneering design to simultaneously observe a broad range of CO transitions in spectral imaging mode which enables the derivation of physical properties of

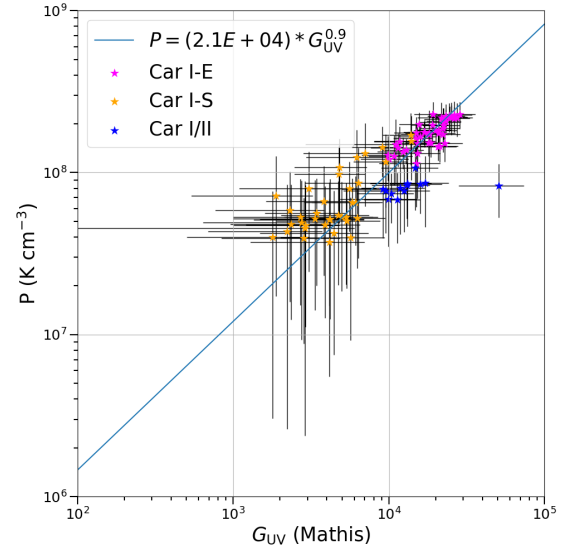


Fig. 13: Relationship between the derived P and G_{UV} for our FOV. The solid blue line shows the empirical power-law relationship between P and G_{UV} values.

molecular gas in a macroscopic field of view. Combined with the state-of-the-art Meudon PDR models, we obtain the following results:

1. The CO emission is observed in the Carina Nebula, near the young star cluster, Trumpler 14, from J = 4 – 3 to J = 13 – 12 across the Car I-E, Car I-S and Car I/II regions (Figure 2 and figures in the Appendix). In the Car I-E region at the northwest of our FOV, the intensities of the observed CO are generally higher by one order of magnitude than those observed in Car I-S and Car I/II. Beyond J = 10 – 9, the emission is concentrated in the Car I-E and locally in the Car I/II regions, hinting higher excitation temperatures of CO gas in these regions.
2. We successfully account for the observed CO and [C I] emission with high pressure and high FUV illumination PDR models. Comparing with previous PDR modeling results found in the same region, the G_{UV} values derived in this work are generally higher (Brooks et al. 2003; Mizutani et al. 2004; Kramer et al. 2008; Oberst et al. 2011). However, the excellent relationship observed between the model-derived G_{UV} values with the estimated radiation fields (Figure 9) from nearby stellar compositions suggest the reliability of the derived G_{UV} values presented in this work. In correspondence with the derived G_{UV} values, the estimated thermal pressure is of the order of magnitude $\sim 10^8 \text{ K cm}^{-3}$. With the modeling results, we confirm that the chief energy sources for the observed CO emissions are the UV-photons and stellar feedback provided by the massive stars in the vicinity.
3. Although the observed ¹²CO, [C I], and [O I] 145 μm transitions can be well accounted for with the Meudon PDR models, direct comparisons of the model-predicted intensities to the observed ¹³CO, [O I] 63 μm , and [C II] 158 μm intensities are not straightforward. Caution is urged when constraining the physical conditions of PDRs with combinations of ¹²CO, ¹³CO, [C I], [O I] 63 μm , and [C II] 158 μm observations.
4. The thermal pressure derived in this work is of the order of magnitude 10^8 K cm^{-3} across our FOV, with the highest values found at the dissociation front in the Car I-E region. Although the spatial resolution of our observa-

tions prevents us from obtaining a detailed cloud structure at the dissociation front, our results are in general agreement with the recent ALMA observations of the Orion Bar that the observed cloud edge is compressed by a high-pressure ($2 \times 10^8 \text{ K cm}^{-3}$) wave propagating into the molecular cloud (Goicoechea et al. 2016; Goicoechea et al. 2017).

5. We find a relation between the thermal pressure at the edge of the PDR and the intensity of the FUV radiation field, $P \sim 2 \times 10^4 G_{UV}$. This relation is similar to the one found by Wu et al. (2015) and Joblin et al. (to be submitted). It suggests that massive stars may create a high pressure slab at the edge of PDRs.
6. Two local ($\sim 0.2 \times 0.2 \text{ pc}$) regions in our FOV deserve further investigation with higher-resolution observations: (1) At the very edge of our FOV (10:43:23.25, -59:33:56.9), a massive class I YSO, V723 Car has been observed to go into outburst just before 2003 (Tapia et al. 2015). All ^{12}CO transitions covered by the *Herschel* SPIRE/FTS and ^{13}CO , up to $J = 8 - 7$, is unambiguously detected here. Unfortunately, we cannot derive the physical conditions from this location due to the variation of instrument resolution, but it will be an interesting target for understanding the interplay between the formation of massive YSOs and their host environment. (2) In the Car I/II region, we find a high G_{UV} values ($\sim 5 \times 10^4$) locally at (10:44:03.89, -59:37:57.63). At this position, CO emission is well detected up to $J = 12 - 11$, and the LTE-approximated T_{ex} value also implies locally excited gas. We cannot identify the possible heating source(s) based on the available observations. To further understand the local heating mechanisms at these locations, high-resolution observations from the region is necessary.

Acknowledgements

- We offer our sincere gratitude to Dr. I. Sakon, Dr. D. Ishihara, Dr. T. Shimonishi, Dr. R. Ohsawa, and, Dr. K. Arimatsu for their success in obtaining the *Herschel* observations presented in this work and to Dr. T. I. Mori for investing her time in the ISO data analysis. The authors sincerely thank Dr. D. Rebollo for sharing the *Mopra* data, Dr. C. Kramer for sharing the *NANTEN2* data, Dr. L. K. Townsley and Dr. P. Broos for sharing the *Chandra* data, and Dr. T. Preibisch for sharing the *Herschel* photometry data. We thank Dr. A. Heayes and Dr. S. Hony for useful discussions.
- This research was supported in part by the Grant-in-Aid for Scientific Research for the Japan Society of Promotion of Science (140500000638), the PRC 1311 between France (CNRS) and Japan (JSPS), the Agence Nationale de la Recherche (ANR) through the programme SYMPATICO (Program Blanc Projet (NR-11-BS56-0023), the Programme National Physique et Chimie du Milieu Interstellaire (PCMI) of CNRS/INSU with INC/INP co-funded by CEA and CNES, and the EU FP7 project DustPedia (Grant No. 606847).
- This research has made use of the SIMBAD database (Wenger et al. 2000) and the VizieR catalogue access tool (Ochsenbein et al. 2000), operated at CDS, Strasbourg, France.

References

Agúndez, M., Goicoechea, J. R., Cernicharo, J., Faure, A., & Roueff, E. 2010, *ApJ*, 713, 662
 Alexander, M. J., Hanes, R. J., Povich, M. S., & McSwain, M. V. 2016, *ApJ*, 152, 190

Allers, K. N., Jaffe, D. T., Lacy, J. H., Draine, B. T., & Richter, M. J. 2005, *ApJ*, 630, 368
 Andree-Labsch, S., Ossenkopf-Okada, V., & Röllig, M. 2017, *A&A*, 598, A2
 Apellániz, J. M., Sota, A., Arias, J. I., et al. 2016, *A&AS*, 224, 4
 Bakes, E. L. O. & Tielens, A. G. G. M. 1994, *ApJ*, 427, 822
 Bertoldi, F. 1989, *ApJ*, 346, 735
 Bertoldi, F. & Draine, B. T. 1996, *ApJ*, 458, 222
 Bohlin, R. C., Savage, B. D., & Drake, J. F. 1978, *ApJ*, 224, 132
 Bron, E., Le Bourlot, J., & Le Petit, F. 2014, *A&A*, 569, A100
 Bron, E., Le Petit, F., & Le Bourlot, J. 2016, *A&A*, 588, A27
 Brooks, K. J., Cox, P., Schneider, N., et al. 2003, *A&A*, 412, 751
 Brooks, K. J., Garay, G., Nielbock, M., Smith, N., & Cox, P. 2005, *ApJ*, 634, 436
 Carraro, G., Romaniello, M., Ventura, P., & Patat, F. 2004, *A&A*, 418, 525
 Chevance, M., Madden, S. C., Lebouteiller, V., et al. 2016, *A&A*, 590, A36
 Cuadrado, S., Goicoechea, J. R., Pilleri, P., et al. 2015, *A&A*, 575, A82
 Federman, S. R., Glassgold, A. E., & Kwan, J. 1979, *ApJ*, 227, 466
 Gagné, M., Fehon, G., Savoy, M. R., et al. 2011, *A&AS*, 194, 5
 Gardner, F. F. & Morimoto, M. 1968, *Austr. J. Phys.*, 21, 881
 Goicoechea, J. R., Chavarría, L., Cernicharo, J., et al. 2015, *ApJ*, 799, 102
 Goicoechea, J. R., Cuadrado, S., Pety, J., et al. 2017, *A&A*, 601, L9
 Goicoechea, J. R. & Le Bourlot, J. 2007, *A&A*, 467, 1
 Goicoechea, J. R., Pety, J., Cuadrado, S., et al. 2016, *Nature*, 537, 207
 Goicoechea, J. R., Teyssier, D., Etxaluze, M., et al. 2015, *ApJ*, 812, 75
 Gonzalez Garcia, M., Le Bourlot, J., Le Petit, F., & Roueff, E. 2008, *A&A*, 485, 127
 Greve, T. R., Leonidaki, I., Xilouris, E. M., et al. 2014, *ApJ*, 794, 142
 Griffin, M. J., Abergel, A., Abreu, A., et al. 2010, *A&A*, 518, L3
 Gry, C., Boulanger, F., Nehmé, C., et al. 2002, *A&A*, 391, 675
 Guzmán, V. V., Goicoechea, J. R., Pety, J., et al. 2013, *A&A*, 560, A73
 Guzmán, V. V., Pety, J., Gratier, P., et al. 2014, *Faraday Discussions*, 168, 103
 Habing, H. J. 1968, *Bull. Astron. Inst. Netherlands*, 19, 421
 Hailey-Dunsheath, S., Sturm, E., Fischer, J., et al. 2012, *ApJ*, 755, 57
 Hamann, W.-R., Gräfener, G., & Liermann, A. 2006, *A&A*, 457, 1015
 Harvey, P. M., Hoffmann, W. F., & Campbell, M. F. 1979, *ApJ*, 227, 114
 Heyminck, S., Graf, U. U., Güsten, R., et al. 2012, *A&A*, 542, L1
 Hogerheijde, M. R., Jansen, D. J., & van Dishoeck, E. F. 1995, *A&A*, 294, 792
 Hur, H., Sung, H., & Bessell, M. S. 2012, *ApJ*, 143, 41
 Indriolo, N., Bergin, E. A., Goicoechea, J. R., et al. 2017, *ApJ*, 836, 117
 Jura, M. 1974, *ApJ*, 191, 375
 Kamenetzky, J., Rangwala, N., Glenn, J., Maloney, P. R., & Conley, A. 2016, *ApJ*, 829, 93
 Kaufman, M. J., Wolfire, M. G., & Hollenbach, D. J. 2006, *ApJ*, 644, 283
 Kaufman, M. J., Wolfire, M. G., Hollenbach, D. J., & Luhman, M. L. 1999, *ApJ*, 527, 795
 Köhler, M., Habart, E., Arab, H., et al. 2014, *A&A*, 569, A109
 Kramer, C., Cubick, M., Röllig, M., et al. 2008, *A&A*, 477, 547
 Le Bourlot, J., Le Petit, F., Pinto, C., Roueff, E., & Roy, F. 2012, *A&A*, 541, A76
 Le Petit, F., Nehme, C., Le Bourlot, J., & Roueff, E. 2006, *ApJS*, 164, 506
 Leurini, S., Wyrowski, F., Wiesemeyer, H., et al. 2015, *A&A*, 584, A70
 Lis, D. C. & Schilke, P. 2003, *ApJ*, 597, L145
 Liseau, R., Justtanont, K., & Tielens, A. G. G. M. 2006, *A&A*, 446, 561
 Malhotra, S., Kaufman, M. J., Hollenbach, D., et al. 2001, *ApJ*, 561, 766
 Marconi, A., Testi, L., Natta, A., & Walmsley, C. M. 1998, *A&A*, 330, 696
 Martins, F., Schaefer, D., & Hillier, D. J. 2005, *A&A*, 436, 1049
 Mathis, J. S., Mezger, P. G., & Panagia, N. 1983, *A&A*, 128, 212
 Mathis, J. S., Rimpl, W., & Nordsieck, K. H. 1977, *ApJ*, 217, 425
 McGee, R. X. & Gardner, F. F. 1968, *Austr. J. of Phys.*, 21, 149
 Meixner, M. & Tielens, A. G. G. M. 1993, *ApJ*, 405, 216
 Mizutani, M., Onaka, T., & Shibai, H. 2004, *A&A*, 423, 579
 Nagy, Z., Van der Tak, F. F. S., Ossenkopf, V., et al. 2013, *A&A*, 550, A96
 Ngoumou, J., Preibisch, T., Ratzka, T., & Burkert, A. 2013, *ApJ*, 769, 139
 Oberst, T. E., Parshley, S. C., Nikola, T., et al. 2011, *ApJ*, 739, 100
 Ochsenbein, F., Bauer, P., & Marcout, J. 2000, *A&AS*, 143, 23
 Okada, Y., Requena-Torres, M. A., Güsten, R., et al. 2015, *A&A*, 580, A54
 Onaka, T., Roellig, T. L., Okada, Y., & Chan, K.-W. 2008, *ASP Conference Series*, 381, 80
 Pabst, C. H. M., Goicoechea, J. R., Teyssier, D., et al. 2017, *A&A*, 606, A29
 Parikka, A., Habart, E., Bernard-Salas, J., et al. 2017, *A&A*, 599, A20
 Parmar, P. S., Lacy, J. H., & Achtermann, J. M. 1991, *ApJ*, 372, L25
 Pecaut, M. J. & Mamajek, E. E. 2013, *A&AS*, 208, 9
 Pérez-Beaupuits, J. P., Wiesemeyer, H., Ossenkopf, V., et al. 2012, *A&A*, 542, L13
 Pilbratt, G. L., Riedinger, J. R., Passvogel, T., et al. 2010, *A&A*, 518, L1
 Pires, A. M., Motch, C., Turolla, R., et al. 2015, *A&A*, 583, A117
 Poglitsch, A., Waelkens, C., Geis, N., et al. 2010, *A&A*, 518, L2
 Pound, M. W. & Wolfire, M. G. 2008, *ASP Conference Series*, 394, 654
 Povich, M. S., Smith, N., Majewski, S. R., et al. 2011, *A&AS*, 194, 14
 Rathborne, J. M., Burton, M. G., Brooks, K. J., et al. 2002, *MNRAS*, 331, 85
 Rebollo, D., Burton, M., Green, A., et al. 2016, *MNRAS*, 456, 2406
 Retallack, D. S. 1983, *MNRAS*, 204, 669
 Robitaille, T. P., Tollerud, E. J., Greenfield, P., et al. 2013, *A&A*, 558, A33

- Röllig, M., Ossenkopf, V., Jeyakumar, S., Stutzki, J., & Sternberg, A. 2006, A&A, 451, 917
- Rosenberg, M. J. F., van der Werf, P. P., Aalto, S., et al. 2015, ApJ, 801, 72
- Sana, H., Momany, Y., Gieles, M., et al. 2010, A&A, 515, A26
- Smith, N. 2006a, MNRAS, 367, 763
- Smith, N. 2006b, ApJ, 644, 1151
- Smith, N. & Brooks, K. J. 2007, MNRAS, 379, 1279
- Smith, N., Egan, M. P., Carey, S., et al. 2000, ApJ, 532, L145
- Sota, A., Apellániz, J. M., Morrell, N. I., et al. 2014, ApJS, 211, 10
- Sternberg, A. & Dalgarno, A. 1989, ApJ, 338, 197
- Stock, D. J., Wolfire, M. G., Peeters, E., et al. 2015, A&A, 579, A67
- Stutzki, J. & Guesten, R. 1990, ApJ, 356, 513
- Swinyard, B. M., Polehampton, E. T., Hopwood, R., et al. 2014, MNRAS, 440, 3658
- Tapia, M., Persi, P., Bohigas, J., Roth, M., & Gomez, M. 2006, MNRAS, 367, 513
- Tapia, M., Roth, M., & Persi, P. 2015, MNRAS, 446, 4088
- Tapia, M., Roth, M., Vazquez, R. A., & Feinstein, A. 2003, MNRAS, 339, 44
- Tauber, J. A., Tielens, A. G. G. M., Meixner, M., & Goldsmith, P. F. 1994, ApJ, 422, 136
- Tielens, A. G. G. M. & Hollenbach, D. 1985, ApJ, 291, 722
- Townsley, L. K., Broos, P. S., Chu, Y.-H., et al. 2011, ApJS, 194, 15
- Vazquez, R. A., Baume, G., Feinstein, A., & Prado, P. 1996, A&AS, 116, 75
- Visser, R., van Dishoeck, E. F., & Black, J. H. 2009, A&A, 503, 323
- Wenger, M., Ochsenbein, F., Egret, D., et al. 2000, A&AS, 143, 9
- Whiteoak, J. B. Z. 1994, ApJ, 429, 225
- Wu, R., Madden, S. C., Galliano, F., et al. 2015, A&A, 575, A88
- Wu, R., Polehampton, E. T., Etxaluze, M., et al. 2013, A&A, 556, A116
- Yıldız, U. A., van Dishoeck, E. F., Kristensen, L. E., et al. 2010, A&A, 521, L40
- Young Owl, R. C., Meixner, M. M., Wolfire, M., Tielens, A. G. G. M., & Tauber, J. 2000, ApJ, 540, 886

Appendix A: Line maps observed by the *Herschel* SPIRE FTS in M83

We show the observed maps of the lines listed in Table 2 by the SPIRE FTS. All the maps are displayed in the observed spatial resolution and in units of $\text{W m}^{-2} \text{sr}^{-1} \text{GHz}^{-1}$ (line profile maps) and $\text{W m}^{-2} \text{sr}^{-1}$ (integrated intensity maps).

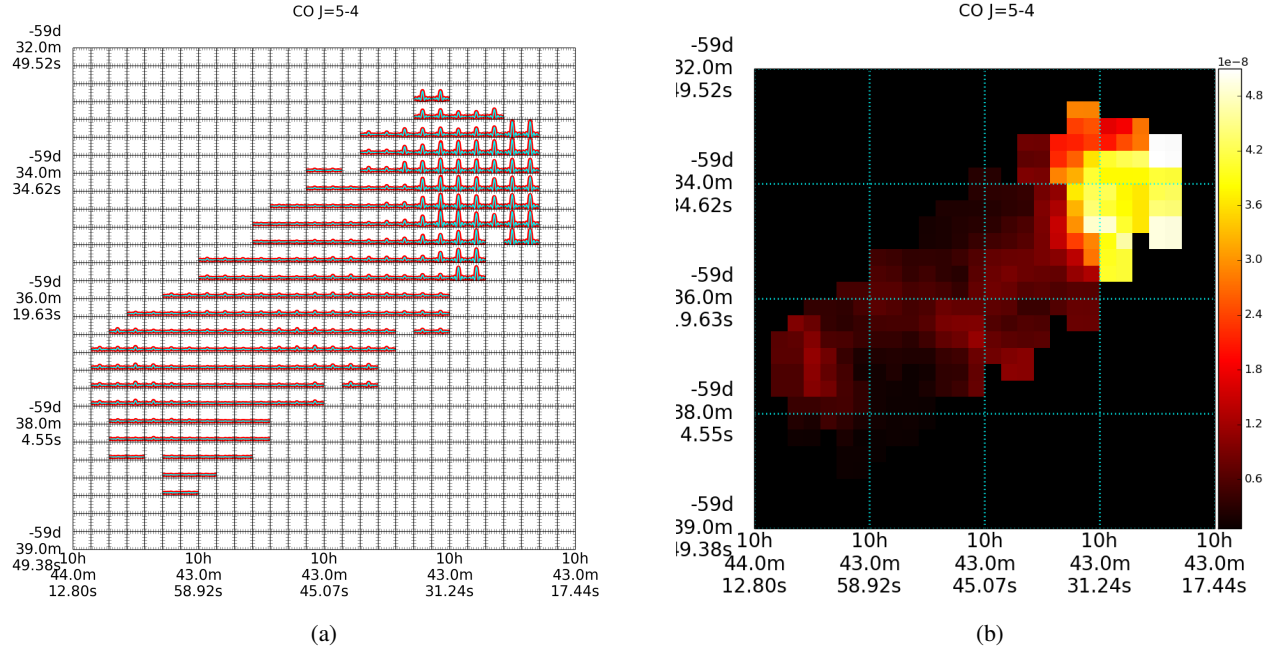


Fig. A.1: Illustration of the spatial distribution of the observed CO J = 5 - 4 line. The left panel shows the continuum-removed coadded spectrum on every pixel within a range of $568 < \nu < 582$ GHz. The vertical axis in each pixel ranges between -1.0×10^{-17} and $5.2 \times 10^{-17} \text{ W m}^{-2} \text{ sr}^{-1} \text{ Hz}^{-1}$. The color map on the right is in units of $\text{W m}^{-2} \text{ sr}^{-1}$.

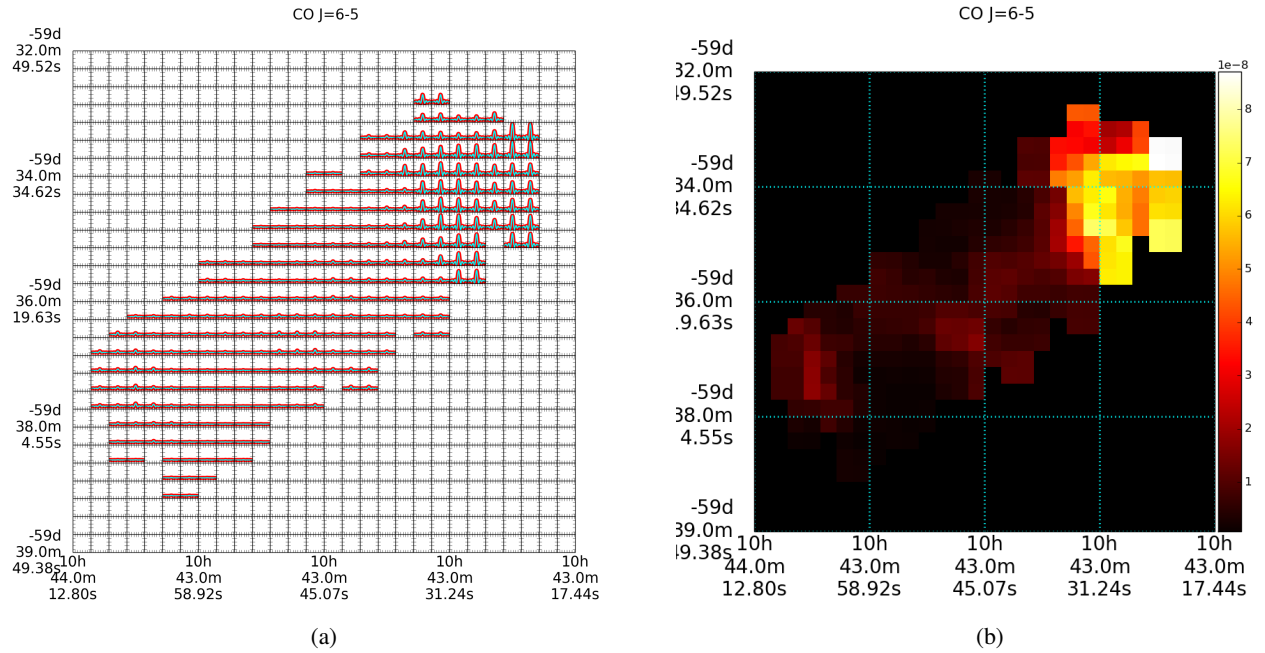


Fig. A.2: Illustration of the spatial distribution of the observed CO J = 6 - 5 line. The left panel shows the continuum-removed coadded spectrum on every pixel within a range of $683 < \nu < 698$ GHz. The vertical axis in each pixel ranges between -8.0×10^{-17} and $8.8 \times 10^{-16} \text{ W m}^{-2} \text{ sr}^{-1} \text{ Hz}^{-1}$. The color map on the right is in units of $\text{W m}^{-2} \text{ sr}^{-1}$.

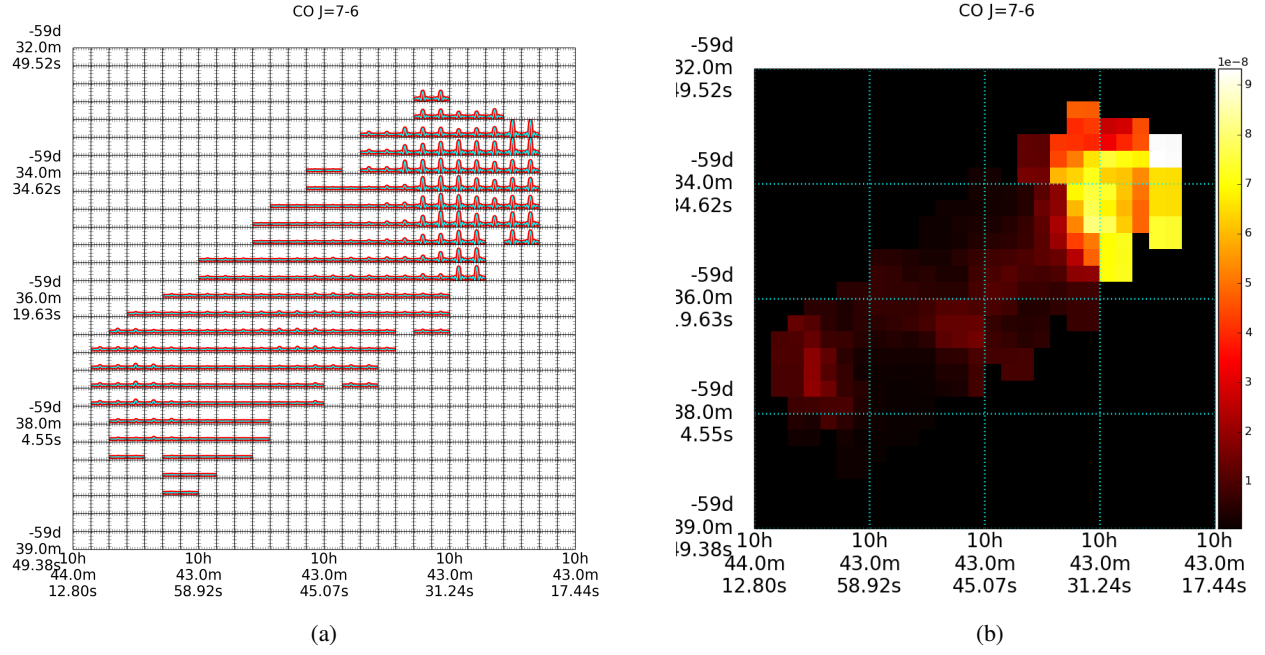


Fig. A.3: Illustration of the spatial distribution of the observed CO J = 7 - 6 line. The left panel shows the continuum-removed coadded spectrum on every pixel within a range of $798 < \nu < 813$ GHz. The vertical axis in each pixel ranges between -2.0×10^{-17} and $1.0 \times 10^{-16} \text{ W m}^{-2} \text{ sr}^{-1} \text{ Hz}^{-1}$. The color map on the right is in units of $\text{W m}^{-2} \text{ sr}^{-1}$.

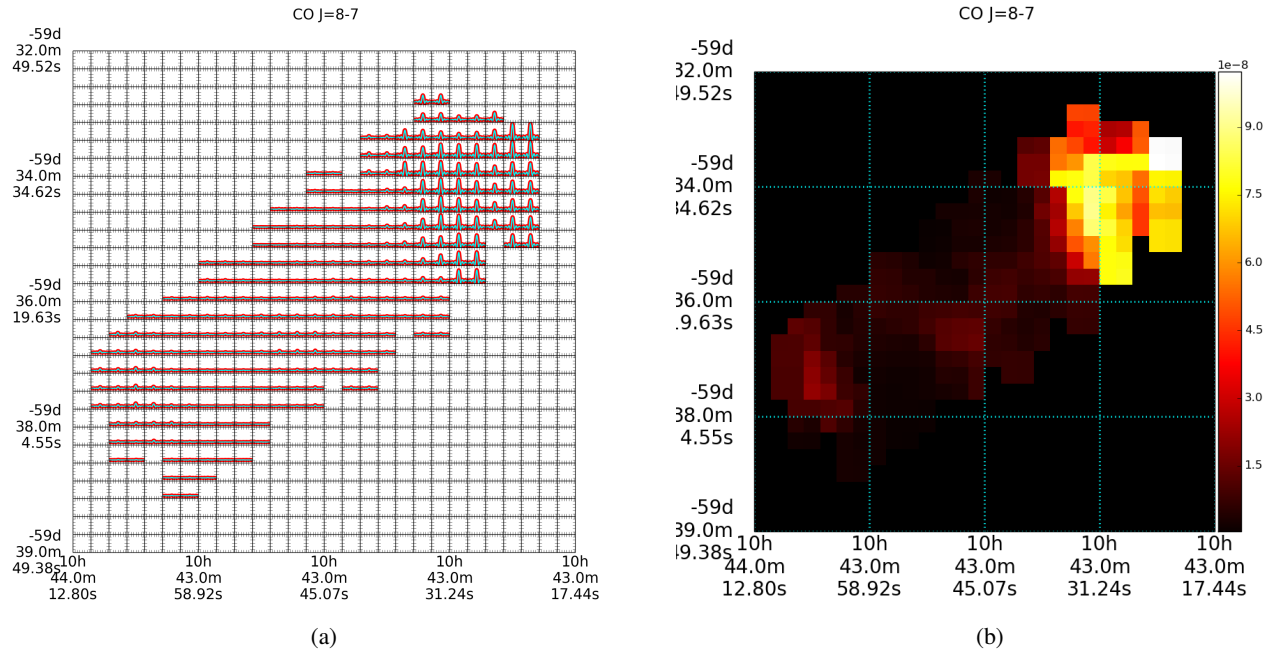


Fig. A.4: Illustration of the spatial distribution of the observed CO J = 8 - 7 line. The left panel shows the continuum-removed coadded spectrum on every pixel within a range of $913 < \nu < 928$ GHz. The vertical axis in each pixel ranges between -1.0×10^{-17} and $1.0 \times 10^{-16} \text{ W m}^{-2} \text{ sr}^{-1} \text{ Hz}^{-1}$. The color map on the right is in units of $\text{W m}^{-2} \text{ sr}^{-1}$.

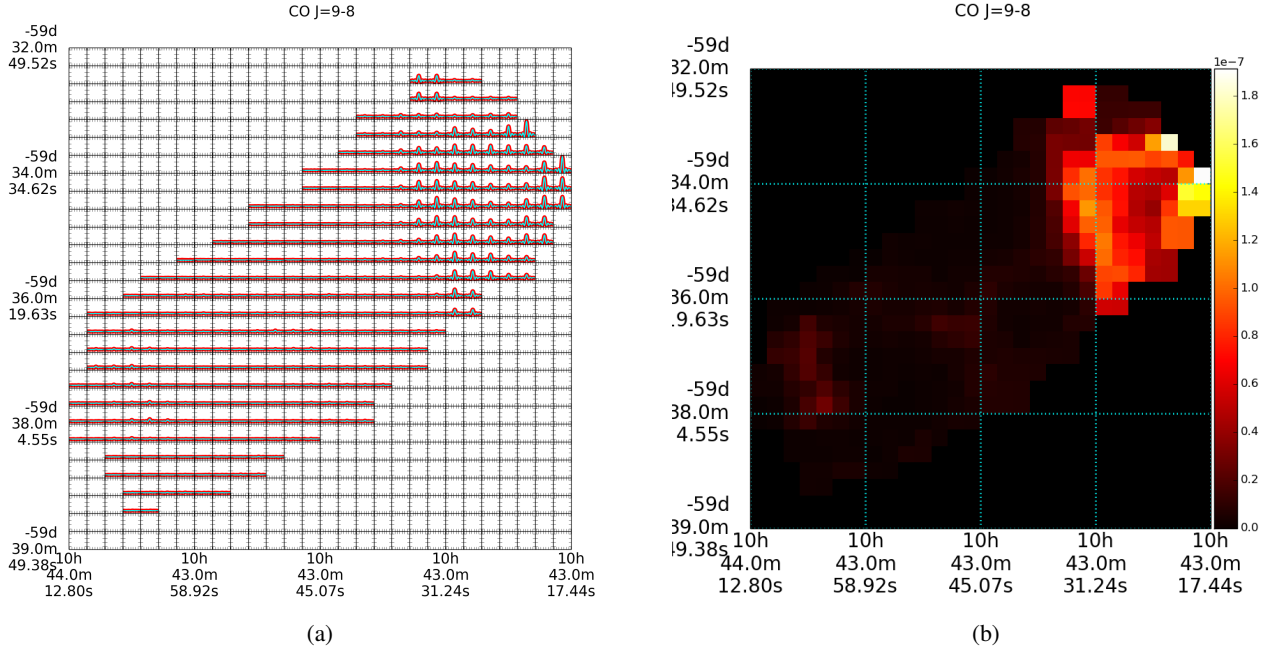


Fig. A.5: Illustration of the spatial distribution of the observed CO J = 9 – 8 line. The left panel shows the continuum-removed coadded spectrum on every pixel within a range of $1028 < \nu < 1042$ GHz. The vertical axis in each pixel ranges between -4.0×10^{-17} and $1.9 \times 10^{-16} \text{ W m}^{-2} \text{ sr}^{-1} \text{ Hz}^{-1}$. The color map on the right is in units of $\text{W m}^{-2} \text{ sr}^{-1}$.

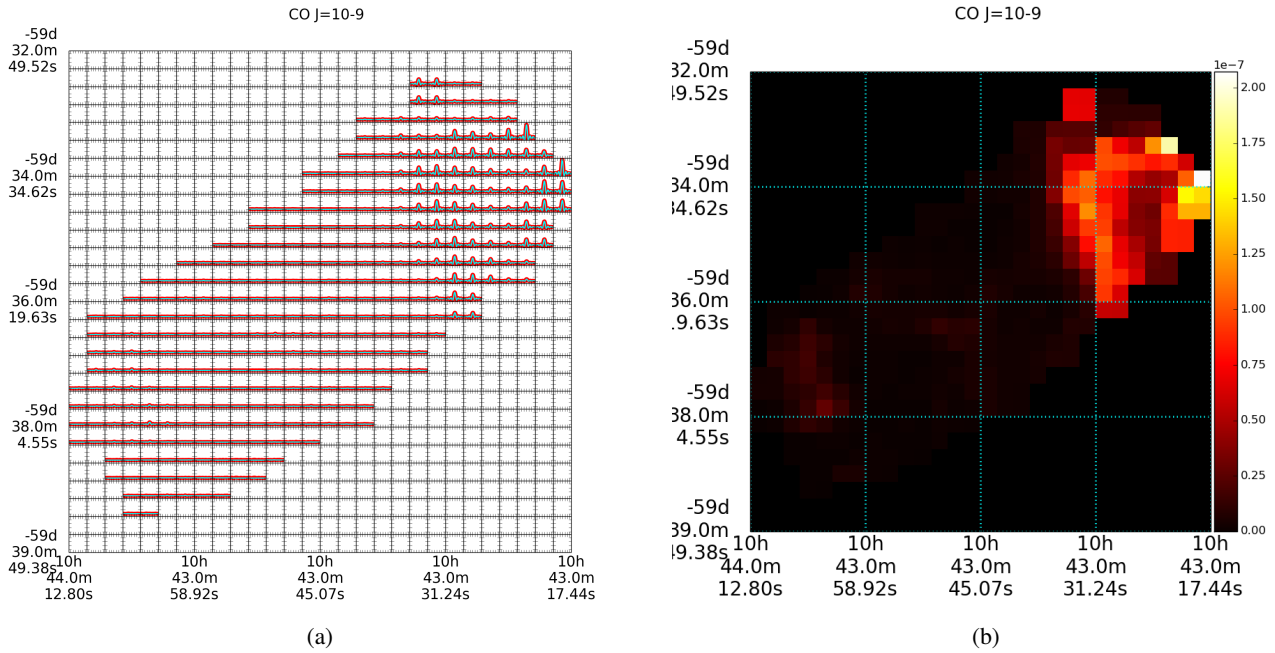


Fig. A.6: Illustration of the spatial distribution of the observed CO J = 10 – 9 line. The left panel shows the continuum-removed coadded spectrum on every pixel within a range of $1143 < \nu < 1157$ GHz. The vertical axis in each pixel ranges between -3.0×10^{-17} and $2.1 \times 10^{-16} \text{ W m}^{-2} \text{ sr}^{-1} \text{ Hz}^{-1}$. The color map on the right is in units of $\text{W m}^{-2} \text{ sr}^{-1}$.

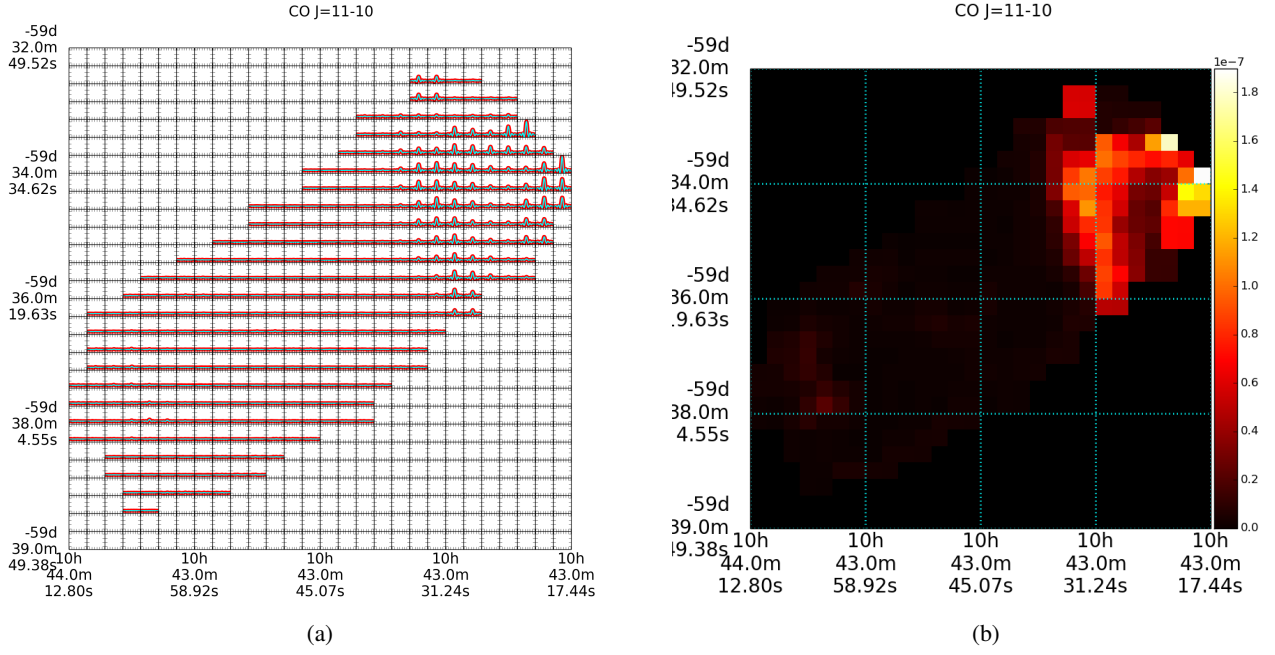


Fig. A.7: Illustration of the spatial distribution of the observed CO J = 11 – 10 line. The left panel shows the continuum-removed coadded spectrum on every pixel within a range of $1258 < \nu < 1272$ GHz. The vertical axis in each pixel ranges between -3.0×10^{-17} and $2.0 \times 10^{-16} \text{ W m}^{-2} \text{ sr}^{-1} \text{ Hz}^{-1}$. The color map on the right is in units of $\text{W m}^{-2} \text{ sr}^{-1}$.

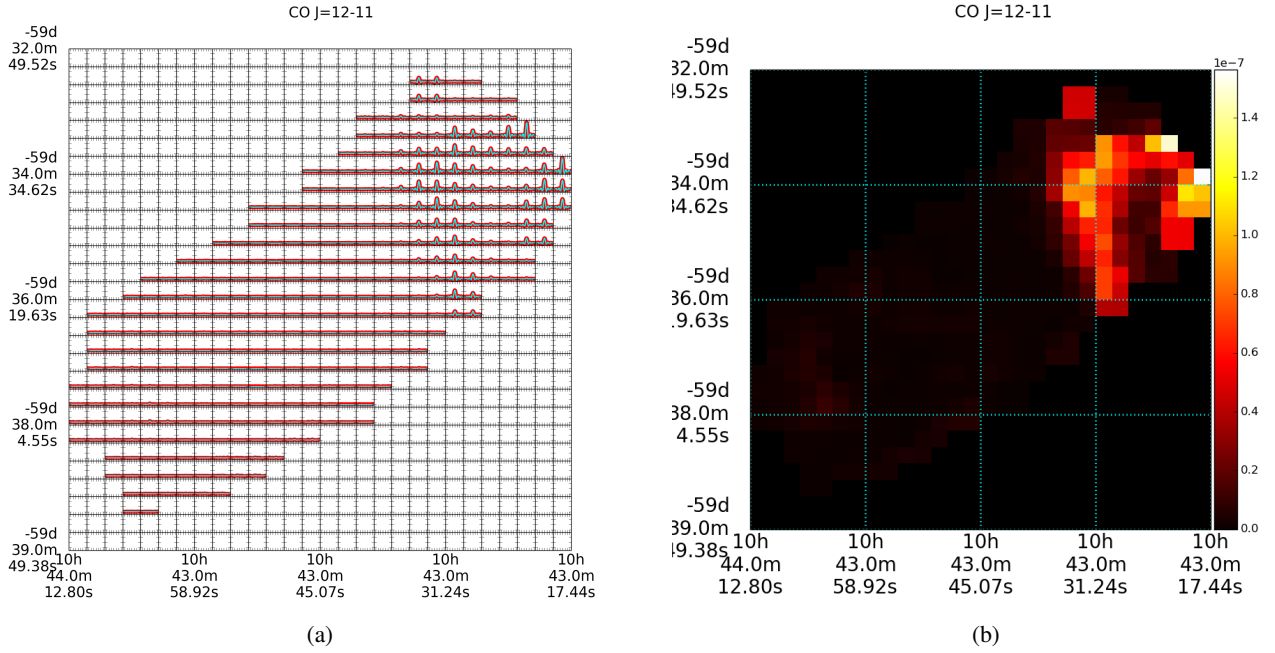


Fig. A.8: Illustration of the spatial distribution of the observed CO J = 12 – 11 line. The left panel shows the continuum-removed coadded spectrum on every pixel within a range of $1372 < \nu < 1387$ GHz. The vertical axis in each pixel ranges between -3.0×10^{-17} and $1.6 \times 10^{-16} \text{ W m}^{-2} \text{ sr}^{-1} \text{ Hz}^{-1}$. The color map on the right is in units of $\text{W m}^{-2} \text{ sr}^{-1}$.

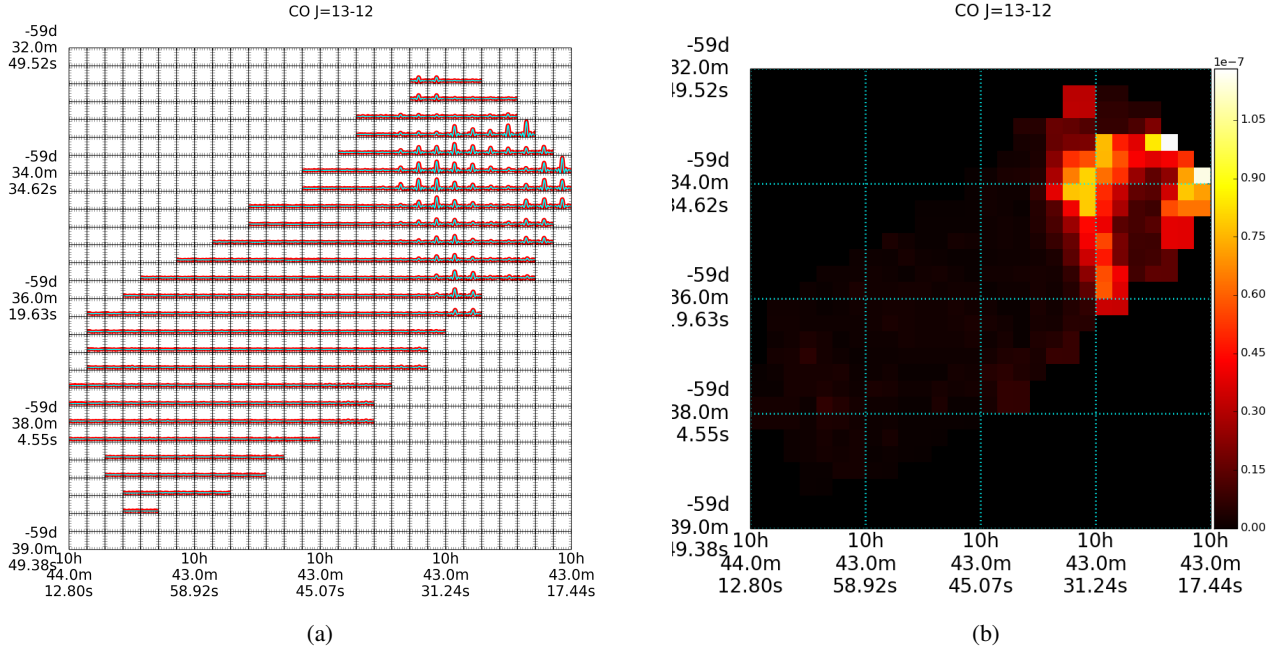


Fig. A.9: Illustration of the spatial distribution of the observed CO J = 13 – 12 line. The left panel shows the continuum-removed coadded spectrum on every pixel within a range of $1487 < \nu < 1502$ GHz. The vertical axis in each pixel ranges between -2.0×10^{-17} and $1.2 \times 10^{-16} \text{ W m}^{-2} \text{ sr}^{-1} \text{ Hz}^{-1}$. The color map on the right is in units of $\text{W m}^{-2} \text{ sr}^{-1}$.

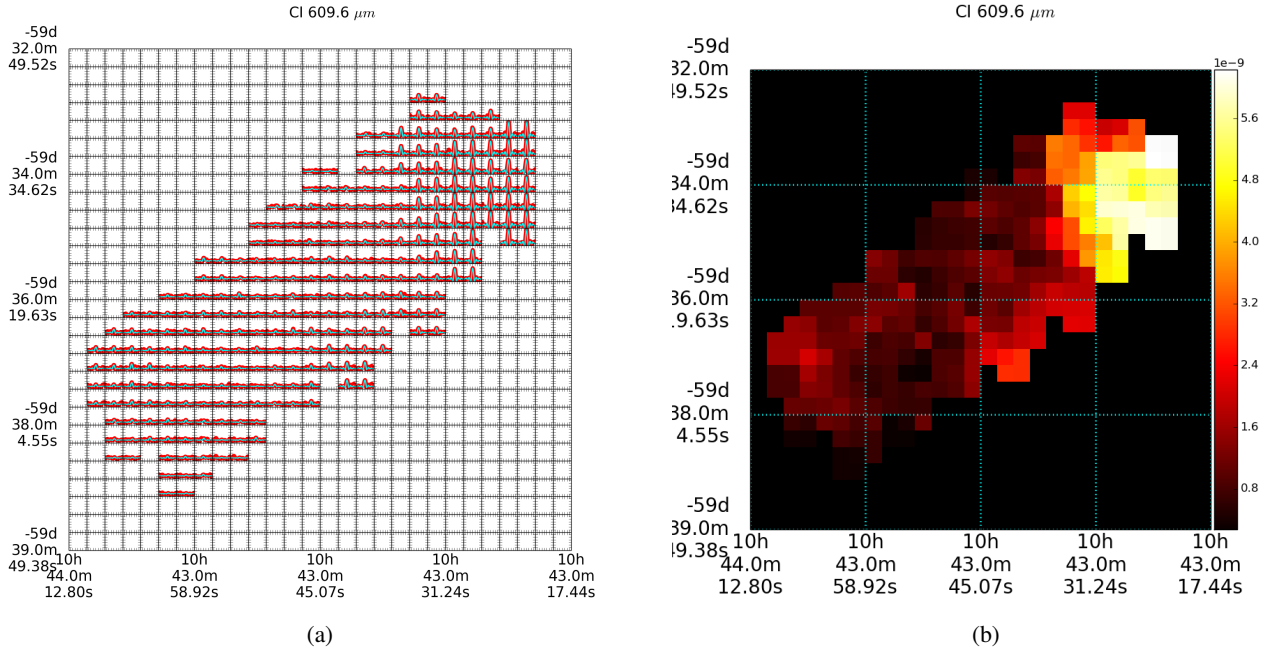


Fig. A.10: Illustration of the spatial distribution of the observed [C] 609 μm line. The left panel shows the continuum-removed coadded spectrum on every pixel within a range of $484 < \nu < 499$ GHz. The vertical axis in each pixel ranges between -1.0×10^{-18} and $6.2 \times 10^{-18} \text{ W m}^{-2} \text{ sr}^{-1} \text{ Hz}^{-1}$. The color map on the right is in units of $\text{W m}^{-2} \text{ sr}^{-1}$.

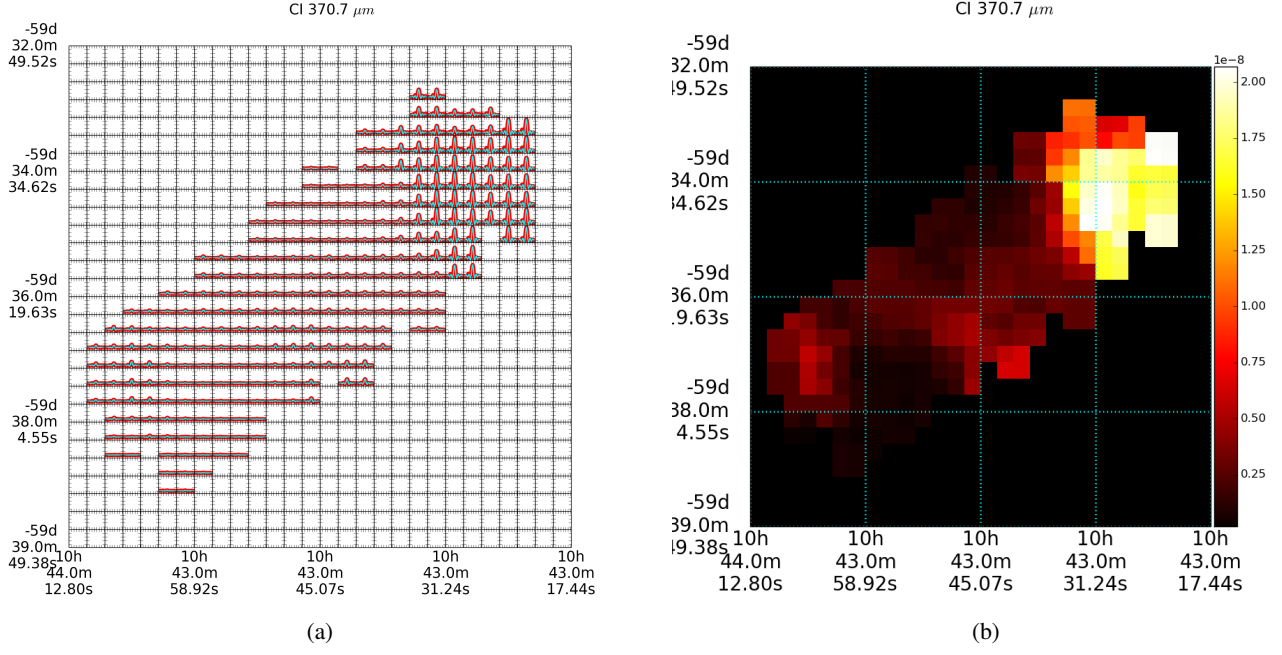


Fig. A.11: Illustration of the spatial distribution of the observed [C I] 370 μm line. The left panel shows the continuum-removed coadded spectrum on every pixel within a range of $801 < \nu < 815$ GHz. The vertical axis in each pixel ranges between -5.0×10^{-18} and $2.2 \times 10^{-17} \text{ W m}^{-2} \text{ sr}^{-1} \text{ Hz}^{-1}$. The color map on the right is in units of $\text{W m}^{-2} \text{ sr}^{-1}$.